OPTOFLUIDIC MICROLASERS BASED ON NON-RADIATIVE ENERGY TRANSFER IN SURFACE-SUPPORTED LIQUID MICRODROPLETS

by

Ersan Özelci

A Thesis Submitted to the
Graduate School of Sciences and Engineering
in Partial Fulfillment of the Requirements for
the Degree of

Master of Science

in

Optoelectronics and Photonics Engineering

Koç University

August, 2014

Koç University

Graduate School of Sciences and Engineering

This is to certify that I have examined this copy of a master's thesis by

Ersan Özelci

and have found that it is complete and satisfactory in all respects,
and that any and all revisions required by the final
examining committee have been made.

Committee Members:

_____

Alper Kiraz, Ph. D.(Advisor)

_____

Alexandr Jonáš, Ph. D.

_____

Kaan Güven, Ph. D.

Date: _____

ABSTRACT

Optofluidics is a recently established research field combining the microfluidic chip technology with optics. It allows for a broad range of applications aiming to develop new photonic devices whose functions are defined by the liquid or to build new integrated photonic devices in which light is used for excitation, analysis, or manipulation of the fluid and the particles in the fluid. In particular, optofluidic lasers hold great promise for developing biological sensors thanks to the high sensitivity of stimulated emission to small perturbations in the laser cavity and gain medium. In an optofluidic dye laser, the gain medium can be directly excited by tuning the pump laser into dye absorption band or non-radiative Förster resonance energy transfer (FRET) can be employed exciting donor molecules which transfer their energy efficiently to acceptor molecules. Optofluidic dye lasers based on FRET enable the extension of the lasing wavelength range and provide new ways of biological sensing thanks to the high sensitivity of FRET efficiency to the donor-acceptor pair separation. In this thesis, the behavior of energy-transfer dye lasers using a mixture of saturable absorber and laser dye as an active medium is investigated theoretically by using rate-equation model. The rate equation model describing the working principle of such dye laser consists of coupled differential equations for the population of energy levels of the dye and the absorber and photon density inside the cavity. Here, we study the temporal characteristics and power of the output lasing pulses as a function of the fluence of the pulsed excitation beam. In the second part, we demonstrate optofluidic microlasers using highly efficient non-radiative FRET for pumping of the gain medium placed within glycerol/water microdroplets situated on a superhydrophobic surface. These droplets can serve as natural microcavities hosting whispering gallery modes (WGMs). Droplets are doped with the FRET donor-acceptor dye pair Rhodamine 6G-Rhodamine 700. FRET lasing is characterized for different acceptor and donor concentrations, and low threshold pump fluences of acceptor lasing are demonstrated. We also verify the nature of the energy transfer (non-radiative vs. radiative) for the range of parameters studied in the experiments.

ÖZETÇE

Optoakışkanlık, optik aygıtları oluşturmak için, sıvıları temel yapı parçası olarak içeren, optik ve mikroakışkanları birleştiren bilimsel ve teknolojik araştırma alanıdır. Optoakışkanlık, optik aygıtları oluşturmak için, sıvıları temel yapı parçası olarak içeren ve işlevleri sıvı tarafından tanımlanmış akışkan içindeki parçacıkların analizini geniş bir uygulama alanına dönüştürür. Özellikle, optofluidik lazerler, lazer çınlaç ve kazanç ortamında uyarılmış ışımanın yüksek hassasiyeti sayesinde biyolojik algılayıcıların gelişiminde önemli yer tutar. Optofluidik lazerlerde, kazanç ortamı direk boya molekülünün uyarılma izgesinde uyarıldığı gibi, verici molekül darbeli lazer ile direk uyarıldıktan sonra, verici ve alıcı moleküller arasındaki yüksek verimli ışımayan çınlayan erk dönüşümü (FRET) sonucu, alıcının ışıma izgesinde lazer ışıması gözlemlenebilir. FRET'e dayalı optofluidik boya lazerler, ışıma dalgaboyunu artırabilir ve biyolojik algılama için yeni yolları bir araya FRETin yüksek hassasiyeti sayesinde getirebilir. Bu tezde, ilk olarak doygun soğuran boya molekülü ve lazer boyası karışımı kullanılarak oluşturulan kazanç ortamıyla oluşturulan boya lazerinin özellikleri hız denklemleri yöntemi kullanılarak kuramsal olarak incelenmiştir. Hız denklemleri yöntemi, iki aynalı boya lazerinin oluşturduğu çınlaçın nasıl çalıstığını ve çınlaç içindeki nüfus yoğunluğu ve foton yoğunluğu diferansiyel denklemlerini tanımlamaktadır. Burada, lazer darbe özelliklerini ve çıkış gücünün giriş gücüne zaman içinde değişimini gösterdik. İkinci bölümde, FRET kazanç ortamı olarak kullanılarak, su tutmayan yüzeylerde gliserol-su karışımı mikrodamlacıklar, optofluidik mikrolazer olarak çalıştırılmışlardır. Bu mikrodamlacıklar fısıldayan geçit kipleri (FGK) barındıran doğal mikroçınlaç olarak optoakışkanlarla tümleşmiştir. FRET'te iki kromofor boya molekülü arasında gerçekleşen erk dönüşüm olgusu ışımadan, verici ve alıcı moleküller arasında dipol-dipol etkisi üzerinden gerçekleşir. Deneyimizde damlacıklar FRET verici-alıcı molekül çifti Rhodamine 6G (R6G)-Rhodamine 700 (R700) ile katkılanmıştır. Farklı derişimlerdeki verici ve alıcı moleküllerle FRET ışıması incelendiğinde, oldukça düşük lazer eşiği elde edilmiştir. Ayrıca değişkenler üzerinde çalışılarak deneyde erk önüşümünün türü doğrulanmıştır.

ACKNOWLEDGMENTS

I would like to thank to my academic advisor, Prof. Alper Kiraz for the guidance and support throughout my research topics. His scientific intuition and comprehension have always been very helpful to solve the problems.

I would like to thank Prof. Alexandr Jonáš and Prof. Kaan Güven for joining my thesis committee. I am also grateful again to Prof. Alexandr Jonáš and Mehdi Aas. I have greatly profited from the experimental and computational skills that they have taught me from beginning of my research. It was a pleasure to work and collaborate with them, and they provided me great insights into different areas.

I would like to thank people from Istanbul Technical University, especially Prof. Cenap Şahabettin Özben and Prof. Tolga Birkandan for their experience, guidance and support for my academics careers in my last year of undergraduate study.

I would like to thank my present and former colleagues, Yasin Karadağ, Asuman Bozkurt Aşıkoğlu, Mustafa Eryürek, Baran Yalçın, Oğuz Kayıllıoğlu, Vahid Pour Reza Ghouschi in Optofluidics and Nano-Optics Research Laboratory.

Additionally, I also want to thank Hayri Can Akyel, Uğur Aygün, M.Necip Aslan, Manuel Boccacani, Mustafa Kılıç, Sezen Ece Önal, Murat Tekşahin, Dalma Forgács and İlker Sevimli for their help, support and endless encouragement friendship to get over most of the problems.

TABLE OF CONTENTS

LIST OF TABLES

LIST OF FIGURES

NOMENCLATURE

Q	Quality Factor
c	Speed of Light
h	Planck Constant
WGM	Whispering Gallery Mode
MDR	Morphology-Dependent Resonance
TE	Transverse Electric
TM	Transverse Magnetic
J_n	Spherical Bessel Function
H_n	Hankel Function
$FWHM$	Full Width at Half Maximum
θ_{inc}	Critical Angle
k	Wave vector
Γ	Emissive Rate of Fluorophore
τ	Decay Time
D	Donor
A	Acceptor
R_0	Förster Radius
τ_D	Decay Time of Donor
N	Avogadro Number
κ	Orientation Factor
E	Efficiency of Energy Transfer
V	Visibility of Interference Pattern
$I_P(t)$	Spatially Averaged Pump Photon Intensity
λ	Wavelength
τ_c	Cavity Decay Time
F_D	Donor Intensity

Chapter 1

INTRODUCTION

1.1 Optofluidics Lasers: Basic Principles and the State of the Art

Optofluidics is exciting research and technology area which combines the advantages of microfluidics and optics to create optical components and systems based on fluids. Fluids have unique properties which cannot be found in classical solid state form of materials, and these properties allow us to design novel devices. Because of their flexibility in shape and refractive index, fluids allow for changing the optical properties of the fluid medium within a device by replacing one fluid with another [1] and optically smooth interfaces can be obtained from the liquid surface tension. Within the past 15 years, the emergence of microfluidics has enabled small-volume sample handling and optical sensing systems evolved to microdevices such as lab-on-a-chip devices, waveguides and resonators for improvement of chemical and biological functionality in lab-on-a-chip analytical systems. Optofluidics has a wide range of integrated applications which include optical communication components, organic dye-based laser light sources [2], or biological sensing. The main advantages of these integrated systems are their compactness and direct compatibility with chemical and biological specimens.

An optofluidic laser integrates microfluidics with a laser cavity and employs the gain medium suspended in liquid for spectral tunability. An optofluidic laser has three essential components; a gain medium, an optical cavity and a pumping mechanism. The gain medium of an optofluidic laser can contain any luminescent material and the use of fluorescent dyes [3] quantum dots [4], and fluorescent proteins [5] has been demonstrated. In order to obtain optical feedback, different types of cavities compatible with liquid gain medium have been shown, including an optofluidic ring resonator (OFRR) [6] and Fabry-Perot cavities [7]. Optofluidics lasers are typically pumped optically, using an external source of pulsed laser

light such as a Q-switched solid-state laser or an optical parametric oscillator. The lasing threshold is accomplished at specific pump fluence, which depends on the Q-factor of cavity and mixture and the concentration of the gain medium.

Optofuidic biolasers are emerging as a highly sensitive way to detect changes in biological molecules. Biolasers incorporate biological material into the gain medium and contain an optical cavity in a fluidic environment. They are able to use amplification which occurs during lasing to quantify tiny changes in biological processes in the gain medium. In addition, fluorescence from attached fluorescent dyes and proteins is widely used to analyze biomolecules that do not display inherent fluorescence. Emission spectrum and intensity change in response to molecular interactions associated with fluorescent probes, thus generating a sensing signal. Even though spontaneous fluorescence has been successfully used in sensing and detection applications, signal-to-noise ratio is often low. As an alternative way, the stimulated emission can be used to increase sensitivity where the probe molecules are placed directly in a laser cavity to amplify the signal. Hence, signal amplification is provided through optical feedback in the laser cavity (see Fig. 1.1). The laser emission from sample placed in laser cavity features spectral, spatial and temporal characteristics different from spontaneous fluorescence in cuvette. The laser emission typically occurs in specific directions which are determined by laser cavity. Hence, its output intensity is significantly higher than omnidirectional fluorescence light. The output intensity of laser cavity displays noticeable threshold behavior and it has significant influence on sensitivity to the biochemical and biological changes [8].

In a recent demonstration, highly selective detection of single-nucleotide difference between DNA molecules has been reported using OFRR and molecular beacon as a gain medium switchable by the analyte [9]. A perfectly matched (PM) DNA and a single base mismatched (SM) DNA were used with a molecular beacon as a model system (see Fig. 1.2). These DNA samples were incorporated as a laser gain medium. A molecular beacon is a DNA probe with stem-loop structure and a dye and a quencher attached to each end of sequence. Molecular beacon can hybridize both with PM DNA and SM DNA and then a fraction of molecular beacons opens up to generate fluorescence emission. This kind of detection can be defined as "analog" detection where the thermodynamic difference between the ability of PM DNA and SM DNA to open up the molecular beacon is directly reflected in

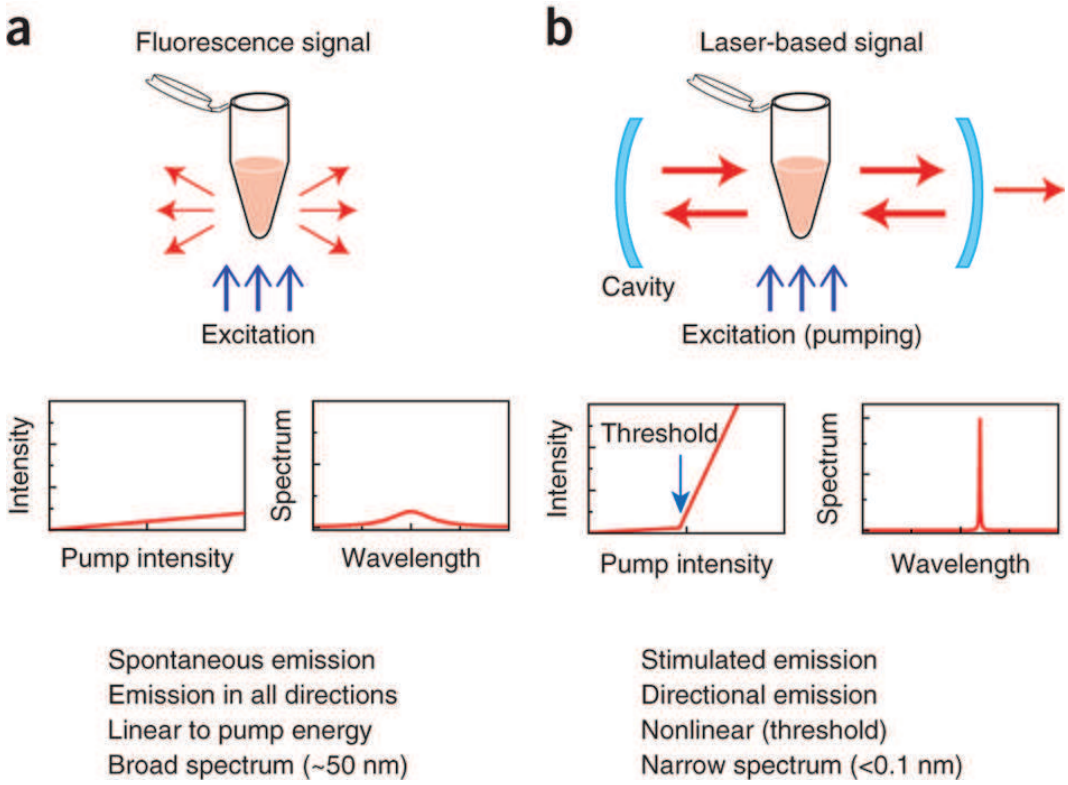

Figure 1.1: Comparison of fluorescence and laser emission detection. (a) Fluorescence emission from a sample in a cuvette. Fluorescence output intensity as a function of the pump intensity and typical broad fluorescence spectrum. (b) Laser emission from the same sample placed inside a laser cavity. Laser output intensity and typical narrowband laser spectrum. Above a threshold intensity, many characteristics of laser emission are different from those of fluorescence emission, including their responses and sensitivities to the biochemical and biological changes occurring in the cuvette. Figure adopted from Ref.[8].

the fluorescence signal intensity. When this system is placed in OFRR where the molecular beacon is the laser gain medium, stimulated emission can occur due to optical feedback from the cavity. If the concentration of open molecular beacons in the cavity is sufficiently high for lasing at the given pump power, emission intensity changes dramatically, thus leading to analog-to-digital conversion in the sensing response. For a pump power carefully chosen to be above the lasing threshold, the presence of the target DNA ensured the operation of the OFRR laser. In contrast, with the same pump power, lasing was not observed and only a negligible fluorescence background was detected when single-base mismatched DNA was added to the gain medium. This analog-to-digital detection scheme revealed an enhancement of over two orders of magnitude in the discrimination ratio between the target and

SM DNA compared to conventional fluorescence hybridization techniques.

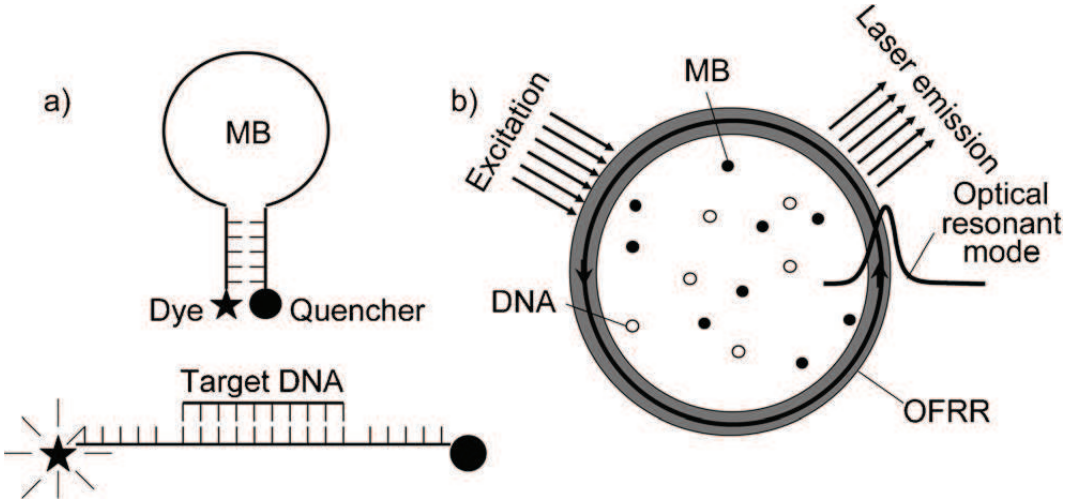

Figure 1.2: (a) Molecular beacon fluorescence is quenched when it is in the closed state. Molecular beacon fluorescence is restored upon hybridization with the target DNA. (b) Molecular beacon and target DNA in the OFRR laser. Figure adopted from Ref.[9].

Various methods of creating optical cavities for integrated optofluidic lasers have been explored such as OFRR, but these functional optical cavities require microfabrication and alignment methods which bring additional experimental difficulties to create optofluidic sensor. In the simplest possible approach for optofluidics laser application, liquid alone can be used to build the resonator without any additional external solid structures. This is enabled by the tendency of liquids to minimize their interface area which transforms small liquid parcels into perfectly spherical droplets (see Fig. 1.3). Such liquid droplets with a typical range of diameters between 5 and 50 microns and refractive index higher than that of the surrounding medium can then serve as alternative self-assembled ring resonators hosting high-quality (high-Q) whispering gallery modes (WGMs) which are confined to small volumes near the droplet rim [10, 11, 12]. The same type of optical resonant modes is also supported by OFRR. However, in contrast to the OFRR where WGMs residing inside the capillary wall interact with the gain medium (or analyte) only through evanescent mode coupling, in a liquid droplet resonator, analytes are placed directly into the cavity. Thus, the analyte molecules that are located near the droplet surface can interact with the peak WGM fields, achieving very strong light-matter coupling. Consequently, high-Q

liquid cavities enable significantly lower threshold for the observation of non-linear optical phenomena -such as lasing or stimulated Raman scattering- than bulk samples.

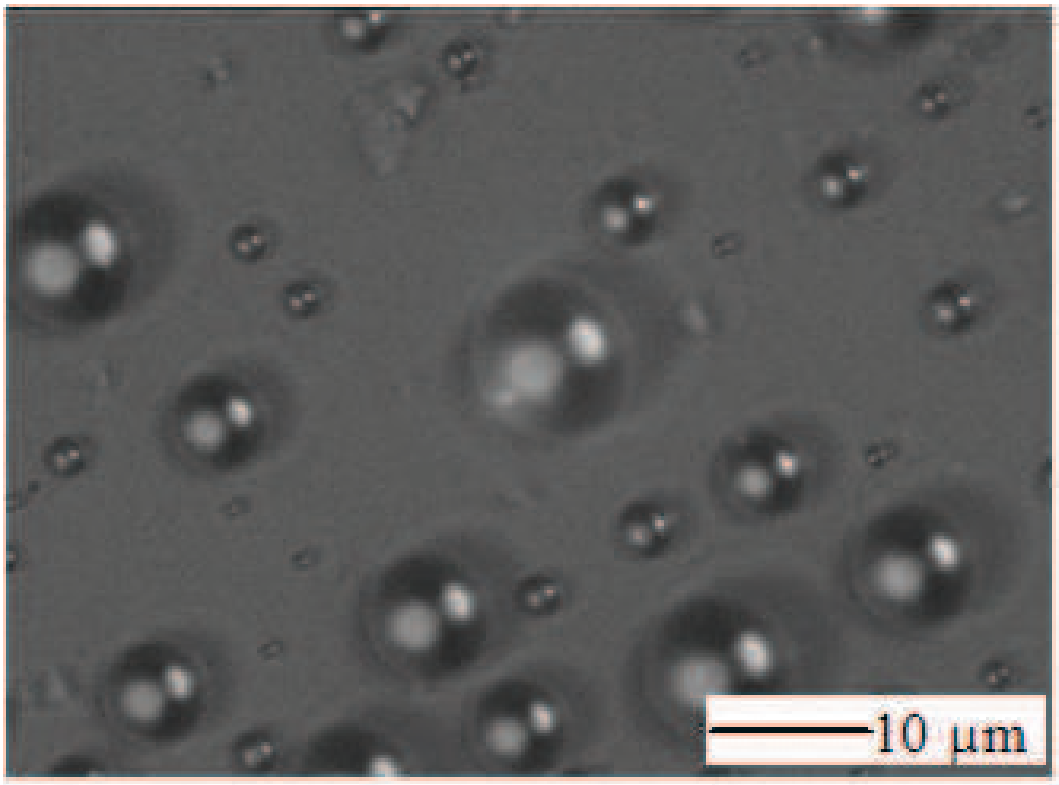

Figure 1.3: The top view of water microdroplets standing on a superhydrophobic surface

Droplet-based optical resonators have found several applications in optofluidics. Optical properties of liquid droplets have been exploited for observation of dye lasing in freely floating aerosols [10], and of Raman lasing [13] and dye-lasing [14] from droplets supported by a superhydrophobic surface. Microdroplets are also attractive for another type of applications which are based on the sensivity of the WGM spectral positions and Q-factors to the microdroplet size as well as the refractive indices of the droplet and surrounding medium. Moreover, aqueous microdroplets provide natural environmental conditions for biological molecules and live cells. These features make microdroplets ideally suited for sensing of biological species [15, 16]. However, droplet-based cavities have only found a limited use in practical sensing applications to date, mostly because of the difficulties with controlling and stabilizing the droplets. Stabilization of droplet position and shape is necessary for mi-

crodroplets applications in optofluidics research. Electrodynamic levitation [17] and optical levitation [18] have been used in optical spectroscopy experiments with individual microdroplets. Although applications exist in chemical and biological analysis, quantum and nonlinear optics, and aerosol science, these techniques were not convenient for integrating with optoelectronic components such as waveguides and fiber optic cables. Solid substrates with superhydrophobic coating preserve the spherical shape of deposited aqueous microdroplets and, thus, allow us to use optical properties of microdroplets in novel lab-on-a-chip optoelectronic devices.

In a dye-doped microdroplet laser, the gain medium is usually excited directly by the pump laser whose wavelength should match the specific dye absorption spectrum. Alternatively, the excitation can be achieved through an energy transfer in dye mixtures which contain the donor and the acceptor. Förster resonance energy transfer (FRET) is a transfer mechanism where the acceptor molecules are excited by the energy transferred in non-radiative way from the directly excited donor molecules by short ranged resonant dipole-dipole interaction [19]. Overlap of the emission spectrum of the donor and the excitation spectrum of the acceptor is necessary for FRET. Efficiency of FRET also depends strongly on the distance between the donor and acceptor molecules. FRET can be quantitatively described by a characteristic separation distance R_0 of the acceptor and donor at which efficiency of non-radiative energy transfer is 50%. For typical dyes, Förster radius, R_0, is between 2 and 10 nm which corresponds to dye concentrations in the μM to mM range. Use of FRET brings several advantages to the design and applications of optofluidic lasers. The energy transfer from donor to acceptor significantly extends the laser emission wavelength range without the need to change any parameter during measurement. Moreover, dye lasers based on energy transfer provide higher pump efficiency and lower lasing threshold than the corresponding single dye lasers due to the low donor absorption loss at the acceptor lasing wavelength. Additionally, suitably chosen donor-acceptor pair can be used in sensing applications of optofluidic lasers to monitor chemical and biological interactions that lead to changes of the donor-acceptor separation distance and, thus, FRET efficiency.

1.2 Thesis Goals and Outline

The aim of this thesis is to develop and characterize optolufluidic microlasers based on energy transfer in liquid microdroplets stabilized by superhydrophobic surface. To this end, the behavior of dye lasers using a mixture of saturable absorber and laser dye as an active medium is first investigated and modeled by using rate-equation model. Subsequently, optofluidic microlasers using highly efficient non-radiative FRET between donor and acceptor molecules for pumping of the gain medium placed within glycerol/water/ethylene glycol microdroplets situated on a superhydrophobic surface are demonstrated and systematically studied.

The main goal of **Chapter 2** is to introduce the concept of whispering gallery modes of spherical resonators. The Mie scattering of a plane wave by a spherical particle is described and then more general case of scattering of an arbitrary beam from the sphere is discussed with the mathematical formulation.

Chapter 3 summarizes basic principles of fluorescence and provides necessary theoretical background for FRET which will be used later in the experimental part of the thesis.

In **Chapter 4**, the characteristics of laser pumped by energy transfer are modeled with rate equations and the dependence of the lasing pulse width and energy on the pump fluence and donor and acceptor concentration is studied.

Chapter 5 presents the experimental procedure and results on FRET lasers based on surface-supported aqueous microdroplets.

Chapter 2

OPTICAL MODES OF A DIELECTRIC SPHERE

2.1 Introduction

The investigation of optical modes of a dielectric sphere is commonly referred to as Mie Scattering Theory, even though Gustav Mie was not the first one to describe this electromagnetic scattering problem. There were other scientists investigating the problem of light scattering by small particles around the turn of the centuries. Alfred Clebsch, solving the elastic scattering problem of a perfectly rigid sphere using potential functions [20], and Ludvig Lorenz [21] contributed to this problem. In 1909, Peter Debye considered the related problem of radiation pressure on a spherical particle [22] utilizing two scalar potential functions like Mie. Hence, scattering of plane wave by a homogeneous isotropic sphere is referred to as Lorenz-Mie theory.

The full electromagnetic wave calculation is necessary to show sharp features of resonant circulation of optical energy in a sphere. These resonances are called whispering gallery modes (WGMs), morphology-dependent resonances (MDRs) or quasi-normal modes (QNMs), and they describe resonance modes of real resonators with finite losses characterized by Q-factor which determines how long photons can be stored inside a resonator. Optical properties of a microsphere depend on the electromagnetic resonant modes of the cavity which will be analyzed in this chapter.

2.2 Theory of Mie Scattering

The scattering of light on spherical objects is a phenomenon which can be seen as the redirection of light taking place when an electromagnetic wave encounters an obstacle. The light scattering theory is categorized in terms of Rayleigh scattering and Mie scattering. Briefly, Rayleigh scattering, named after Lord Rayleigh, refers to the elastic scattering of light for objects that can be described as point dipoles sufficiently smaller than the wavelength of the scattered light [23]. It is an approximation to the more general Mie

scattering that describes interaction between light waves and particles of all sizes. For example, fluctuations of the molecular density of air in the atmosphere of Earth cause Rayleigh scattering of sunlight which is responsible for apparent blue color of the sky. Mie scattering named after Gustave Mie describes the scattering of electromagnetic radiation by a sphere of size generally larger than the radiation wavelength. The Mie scattering depends on size and index of refraction of the scattering particle and on the index of refraction of the medium surrounding the particle [24]. The Mie Theory is the solution of the Maxwell equations including appropriate boundary conditions which requires continuity of magnetic and electric fields on the surface of the sphere [25].

Fig. 2.1 shows the geometry of the system with directions of coordinate axes for description of the scattering of electromagnetic wave by a sphere. The incident wave propagates in the direction of negative z-axis.

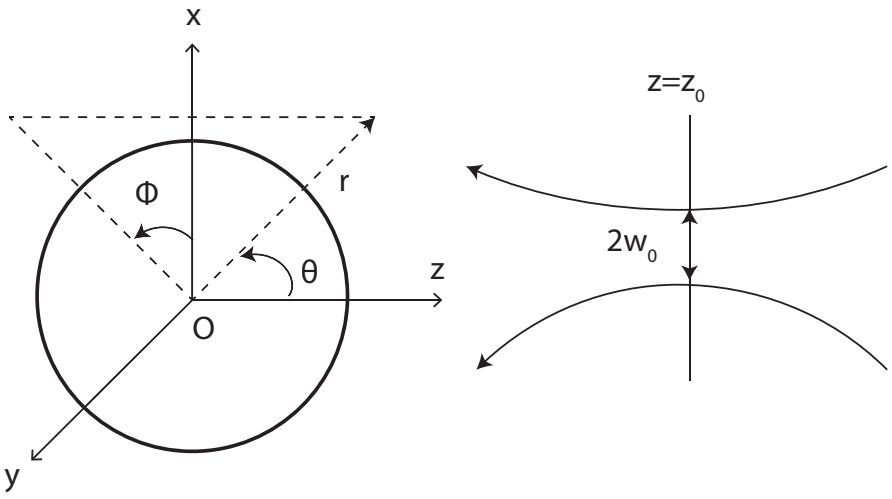

Figure 2.1: Geometry for arbitrary electromagnetic beam incident upon a sphere

Let's assume light scattering of an arbitrary light beam from a spherical particle. Maxwell equations for electromagnetic field $\vec{E}$, $\vec{H}$ in a linear, isotropic, homogeneous medium with zero density of current and free charge are given as

$$\nabla \cdot \vec{E} = 0 \tag{2.1}$$

$$\nabla \cdot \vec{H} = 0 \tag{2.2}$$

$$\nabla \times \vec{E} = i\omega\mu\vec{H} \tag{2.3}$$

$$\nabla \times \vec{H} = -i\omega\epsilon\vec{E} \tag{2.4}$$

where ϵ is the permittivity of the medium, μ is the permeability of the medium, and factor ω comes from the time dependence of the wave expression exp(-iωt). Taking the curl of Eq.(2.3) and combining it with Eq.(2.1) and Eq.(2.4) gives the Helmholtz equation Eq.(2.5) for the electric field. Similarly, taking the curl of Eq.(2.4) and combining it with Eq.(2.2) and Eq.(2.3) gives the Helmholtz equation Eq.(2.6) for the magnetic field:

$$\nabla^2\vec{E} + k^2\vec{E} = 0 \tag{2.5}$$

$$\nabla^2\vec{H} + k^2\vec{H} = 0 \tag{2.6}$$

where $k^2 = \omega^2\mu\epsilon$ is the wave number in the surrounding medium.

We want to obtain a general electromagnetic field solution of Eq.(2.5) and Eq.(2.6) which can relate electromagnetic field expressions for the incident, scattered, and internal electromagnetic fields by applying boundary conditions at the surface of the sphere with radius a. If Eq.(2.3) and Eq.(2.4) are transformed into spherical co-ordinates, their solution can be expressed as the sum of two linearly independent sub-fields ${}^{TE}\vec{E}$, ${}^{TM}\vec{E}$ and ${}^{TE}\vec{H}$, ${}^{TM}\vec{H}$ where the transverse electric (TE) and transverse magnetic (TM) solutions are characterized by the electric field or the magnetic field is parallel to the surface of the sphere, respectively:

$${}^{TE}E_r = 0 \tag{2.7}$$

$${}^{TM}H_r = 0 \tag{2.8}$$

and the boundary conditions are defined as

$$\sum_{k=TE,TM} {}^{k}E_{\theta,int} = \sum_{l=TE,TM} {}^{l}E_{\theta,ext} \tag{2.9}$$

$$\sum_{k=TE,TM} {}^{k}E_{\phi,int} = \sum_{l=TE,TM} {}^{l}E_{\phi,ext} \tag{2.10}$$

$$\sum_{k=TE,TM} {}^{k}H_{\theta,int} = \sum_{l=TE,TM} {}^{l}H_{\theta,ext} \tag{2.11}$$

$$\sum_{k=TE,TM} {}^{k}H_{\phi,int} = \sum_{l=TE,TM} {}^{l}H_{\phi,ext} \tag{2.12}$$

for r=a.

Each of the sub-fields (TM and TE) can be obtained from a single scalar potential ${}^{TM}\Pi$ and ${}^{TE}\Pi$ which are known as Debye's potentials [26]. In terms of the scalar potential associated with the TM field (${}^{TM}\Pi$) and the scalar potential associated with the TE field (${}^{TE}\Pi$) the electromagnetic field components are given for radial component [Eq.(2.13) - Eq.(2.14)] , polar component [Eq.(2.15) - Eq.(2.16)], and azimuthal component [Eq.(2.17) - Eq.(2.18)] as

$$E_r = \frac{\partial^2 \left(r^{TM}\Pi\right)}{\partial r^2} + k^2 r^{TM}\Pi \tag{2.13}$$

$$H_r = \frac{\partial^2 \left(r^{TE}\Pi\right)}{\partial r^2} + k^2 r^{TE}\Pi \tag{2.14}$$

$$E_\theta = \frac{1}{r}\frac{\partial^2 \left(r^{TM}\Pi\right)}{\partial\theta\partial r} + \frac{k^{''}}{r\sin\theta}\frac{\partial \left(r^{TE}\Pi\right)}{\partial\Phi} \tag{2.15}$$

$$H_\theta = -\frac{k^{'}}{r\sin\theta}\frac{\partial \left(r^{TM}\Pi\right)}{\partial\phi} + \frac{1}{r}\frac{\partial^2 \left(r^{TE}\Pi\right)}{\partial r\partial\theta} \tag{2.16}$$

$$E_\phi = \frac{1}{r\sin\theta}\frac{\partial^2 \left(r^{TM}\Pi\right)}{\partial\phi\partial r} - \frac{k^{''}}{r}\frac{\partial \left(r^{TE}\Pi\right)}{\partial\theta} \tag{2.17}$$

$$H_\phi = \frac{k^{'}}{r}\frac{\partial \left(r^{TM}\Pi\right)}{\partial\theta} + \frac{1}{r\sin\theta}\frac{\partial^2 \left(r^{TE}\Pi\right)}{\partial r\partial\phi} \tag{2.18}$$

where $k^{'} = i\omega\epsilon$ and $k^{''} = i\omega\mu$. Both ${}^{TM}\Pi$ and ${}^{TE}\Pi$ satisfy the Helmholtz equation

$$\nabla^2\Pi + k^2\Pi = 0. \tag{2.19}$$

Eq.(2.19) can be solved from assumption that each scalar potential is the product of three functions which depend solely on r, θ and ϕ.

$$\Pi(r,\theta,\phi) = R(r)\Theta(\theta)\Phi(\phi) \tag{2.20}$$

Substituting Eq.(2.20) into Eq.(2.19) gives ordinary differential equations for the azimuthal, the polar and the radial functions, respectively

$$\frac{\partial^2\Phi}{\partial\phi} + m^2\Phi = 0 \tag{2.21}$$

$$\frac{1}{\sin\theta}\frac{\partial}{\partial\theta}(\sin\theta\frac{\partial\Theta}{\partial\theta}) + [l(l+1) - \frac{m^2}{sin^2\theta}]\Theta = 0 \tag{2.22}$$

$$\frac{\partial}{\partial r}(r^2\frac{\partial R}{\partial r}) + [k^2r^2 - l(l+1)]R = 0 \tag{2.23}$$

Their values are restricted by the condition of single-valuedness of the field in arbitrary point in space, so that $l > |m|$ where m and l are integer. General solution can be derived for azimuthal, polar and radial part separately [27]. Radial dependence $rR(r)$ is described by ψ_l and χ_l which are Ricatti-Bessel functions. ψ_l and χ_l are connected to half-integer Bessel functions $J_{l+1/2}$ and $N_{l+1/2}$ by

$$\psi_l(kr) = \sqrt{\frac{\pi kr}{2}}J_{l+1/2}(kr) \tag{2.24}$$

$$\chi_l(kr) = -\sqrt{\frac{\pi kr}{2}}N_{l+1/2}(kr) \tag{2.25}$$

After the normalization, the combination of $\Theta(\theta)$ and $\Phi(\phi)$ gives the spherical harmonic functions

$$Y_{lm}(\theta,\phi) = \sqrt{\frac{2l+l}{4\pi}\frac{(l-m)!}{(l+m)!}}P_l^m(\cos\theta)\exp(im\phi) \tag{2.26}$$

where $P_l^m(\cos\theta)$ are the associated Legendre polynomials. The full solutions of the Helmholtz equation Eq.(2.19) including separation of variables are given as:

$$r\Pi = \sum_{l=0}^{\infty} \sum_{m=-l}^{l} \left[\tilde{A}_{lm} \psi_l (kr) + \tilde{B}_{lm} \chi_l (kr) \right] Y_{lm}(\theta, \phi), \tag{2.27}$$

where $\tilde{A}_{lm}$ and $\tilde{B}_{lm}$ are the arbitrary complex constants. $\tilde{A}_{lm} = \tilde{B}_{lm} = 0$ for $m \neq 1$ for an incident plane wave whereas the expansion coefficients are not zero for other m values in the case of an arbitrary beam.

The TM and TE scalar potentials for the incident field (i), the scattered field (s) and the inside field (w) can be expressed in the form of Eq.(2.27) [28]. For the incident field, χ_l functions which are unbounded at the origin (r=0) must be excluded as the incident field should be describable everywhere in the space including the origin.

$$r^{TM}\Pi_{(i)} = \sum_{l=0}^{\infty} \sum_{m=-l}^{l} A_{lm} \psi_l (k_{ext} r) Y_{lm}(\theta, \phi), \tag{2.28}$$

$$r^{TE}\Pi_{(i)} = \sum_{l=0}^{\infty} \sum_{m=-l}^{l} B_{lm} \psi_l (k_{ext} r) Y_{lm}(\theta, \phi), \tag{2.29}$$

For the scattered field, which takes the form of a diverging spherical wave when r goes infinity it is suitable to choose $\tilde{B}_{lm}$=-$\tilde{A}_{lm}$ that gives

$$r^{TM}\Pi_{(s)} = \sum_{l=0}^{\infty} \sum_{m=-l}^{l} a_{lm} \xi_l^{(1)} (k_{ext} r) Y_{lm}(\theta, \phi), \tag{2.30}$$

$$r^{TE}\Pi_{(s)} = \sum_{l=0}^{\infty} \sum_{m=-l}^{l} b_{lm} \xi_l^{(1)} (k_{ext} r) Y_{lm}(\theta, \phi), \tag{2.31}$$

where $\xi_l^{(1)} = \psi_l$-$i\chi_l$ functions are chosen since these functions correspond to outward traveling spherical waves in the limit of r going to infinity.

Similarly to the incident field, χ_l functions are excluded in the description of the internal field since these functions are unbounded at *r=0*

$$r^{TM}\Pi_{(w)} = \sum_{l=0}^{\infty} \sum_{m=-l}^{l} c_{lm} \psi_l (k_{int} r) Y_{lm}(\theta, \phi), \tag{2.32}$$

$$r^{TE}\Pi_{(w)} = \sum_{l=0}^{\infty} \sum_{m=-l}^{l} d_{lm} \psi_l (k_{int} r) Y_{lm}(\theta, \phi), \tag{2.33}$$

The expansion coefficients of each field are related through boundary conditions which are applied on the external potential (subscript "ext") $\Pi_{ext} = \Pi^i + \Pi^s$ and the potential

inside the sphere (subscript "int") $\Pi_{int} = \Pi^w$. Since the expansion terms in the infinite series for the potentials are independent of each other, boundary conditions must hold for each term in the series which gives the coefficients of the scattered field as

$$a_{lm} = \frac{\psi_l^{'}(k_{int}a)\,\psi_l(k_{ext}a) - \bar{n}\psi_l(k_{int}a)\,\psi_l^{'}(k_{ext}a)}{\bar{n}\psi_l(k_{int}a)\,\xi_l^{(1)'}(k_{ext}a) - \psi_l^{'}(k_{int}a)\,\xi_l^{(1)}(k_{ext}a)} A_{lm}, \tag{2.34}$$

$$b_{lm} = \frac{\bar{n}\psi_l^{'}(k_{int}a)\,\psi_l(k_{ext}a) - \psi_l(k_{int}a)\,\psi_l^{'}(k_{ext}a)}{\psi_l(k_{int}a)\,\xi_l^{(1)'}(k_{ext}a) - \bar{n}\psi_l^{'}(k_{int}a)\,\xi_l^{(1)}(k_{ext}a)} B_{lm}. \tag{2.35}$$

and the coefficients of the internal field as

$$c_{lm} = \frac{\xi_l^{(1)'}(k_{ext}a)\,\psi_l(k_{ext}a) - \xi_l^{(1)}(k_{ext}a)\,\psi_l^{'}(k_{ext}a)}{\bar{n}^2\psi_l(k_{int}a)\,\xi_l^{(1)'}(k_{ext}a) - \bar{n}\psi_l^{'}(k_{int}a)\,\xi_l^{(1)}(k_{ext}a)} A_{lm}, \tag{2.36}$$

$$d_{lm} = \frac{\xi_l^{(1)'}(k_{ext}a)\,\psi_l(k_{ext}a) - \xi_l^{(1)}(k_{ext}a)\,\psi_l^{'}(k_{ext}a)}{\psi_l(k_{int}a)\,\xi_l^{(1)'}(k_{ext}a) - \bar{n}\psi_l^{'}(k_{int}a)\,\xi_l^{(1)}(k_{ext}a)} B_{lm} \tag{2.37}$$

where $\bar{n} = (\bar{\epsilon}_{int}/\epsilon_{ext})^{1/2}$ is the complex relative index of refraction and a is the sphere radius.

In order to determine the coefficients A_{lm} and B_{lm} describing the incident wave, radial components of the electric field and magnetic field $E_r^i(r,\theta,\phi)$ $H_r^i(r,\theta,\phi)$ of the incident wave over the sphere surface are used. $E_r^i(a,\theta,\phi)$ at $r{=}a$ can be expanded in a series of spherical harmonics, which form an orthogonal base, as

$$E_r^i(a,\theta,\phi) = \sum_{l=0}^{\infty}\sum_{m=-l}^{l} \Omega_{lm} Y_{lm}(\theta,\phi) \tag{2.38}$$

where

$$\Omega_{lm} = \int_0^{2\pi}\int_0^{\pi} E_{i,r}(a,\theta,\phi) Y_{lm}^*(\theta,\phi)\sin\theta d\theta d\phi \tag{2.39}$$

Substituting Eq.(2.28) for potential ${}^{TM}\Pi_i$ into Eq.(2.13) for the radial component of the electric field gives

$$E_r^i(a,\theta,\phi) = \frac{1}{a^2}\sum_{l=0}^{\infty}\sum_{m=-l}^{l} [l(l+1)A_{lm}\psi(k_{ext}a)Y_{lm}(\theta,\phi)] \tag{2.40}$$

Finally, A_{lm} can be derived by equating Eq.(2.38) to Eq.(2.40),

$$A_{lm} = \frac{a^2}{l(l+1)\psi_l\left(k_{ext}a\right)} \int_0^{2\pi} \int_0^{\pi} sin\theta E_r^i\left(a,\theta,\phi\right) \times Y_{lm}^* d\theta d\phi, \tag{2.41}$$

The TE wave coefficient.

$$B_{lm} = \frac{a^2}{l(l+1)\psi_l\left(k_{ext}a\right)} \int_0^{2\pi} \int_0^{\pi} sin\theta H_r^i\left(a,\theta,\phi\right) \times Y_{lm}^* d\theta d\phi, \tag{2.42}$$

can be derived by using similar process from the radial component of magnetic field $H_r^i(r,\theta,\phi)$.

2.3 Whispering Gallery Modes

Whispering gallery modes (WGMs) are specific resonances of the wave field in a cavity with circular symmetry. WGMs can be interpreted as electromagnetic waves that circulate around the perimeter of the cavity and are strongly confined within the structure. In terms of geometric optics, the confinement is described by the light rays which are totally internally reflected from the cavity surface (see Fig. 2.2). The resonance condition occurs if, after one round trip, the wave reaches the starting point with the same phase. Then these multiply reflected waves interfere constructively with each other to form standing waves [29].

The term, WGMs, is due to Lord Rayleigh, who studied the characteristics of acoustic wave propagation in the circular gallery, running around the interior of the dome of St Pauls Cathedral in London. In the demonstration, two people standing facing the wall at opposite sides of the room could hear their whispers, but when these people stepped either back or forth from the center of the room, they were not able to hear each other. The demonstration showed that this effect is provided by the smooth, curved walls where the sound waves travel around the room effectively [23]. WGM optical cavities are dielectric structures which trap traveling light around the cavity surface similar to sound waves traveling in a whispering gallery.

Since the optical resonances are a function of the morphology and dielectric properties of the cavity, they can be referred to as MDRs (Morphology-Dependent Resonances) [30]. Due to minimal reflection losses and potentially very low material absorption, these resonances can reach exceptionally high-quality factors up to 10^{11}.

Fig. 2.2 illustrates the concept of resonances associated with WGMs. A ray of light propagates inside the sphere and hits the surface with angle of incidence θ_{inc}. If this angle

of incidence is equal to or greater than the critical angle θ_c total internal reflection (TIR) occurs.

$$\theta_{inc} \geq \theta_c = arcsin(1/\bar{n}(\omega)) \tag{2.43}$$

Here, $\bar{n}(\omega)$ is the relative index of the refraction of the sphere which depends on the angular frequency of the light ω. The resonance condition for a sphere with circumference $2\pi a >> \lambda$ (where λ is the wavelength of light in the medium outside the sphere) and rays propagating with θ_{inc} close to 90^o is shown in Fig. 2.2. Let's assume that at resonance, exactly l wavelengths fit into the closed ray path, corresponding to the resonant mode with polar number l. If we define the sphere size parameter as $x = 2\pi a/\lambda$, the value of x for l-th resonant mode then obeys the following inequality.

$$\frac{l}{\bar{n}(\omega)} \leq \frac{2\pi a}{\lambda} \leq l \tag{2.44}$$

By using the size parameter which is dimensionless the resonance condition can be also defined as

$$x \leq l \leq \bar{n}(\omega)x. \tag{2.45}$$

Optical modes in dielectric sphere were studied in the previous section and the Lorenz-Mie Theory gave analytical solution to the problem of scattering of electromagnetic wave by a sphere of radius a with relative index of refraction $\bar{n}(\omega)$. The WGMs correspond to two linearly independent solutions of wave equation: transverse electric (TE) and transverse magnetic (TM) modes which are completely determined by individual expansion terms in the infinite series of Eq.(2.32) and Eq.(2.33). These modes are characterized by polar mode number, l, which gives approximately the number of wavelengths that fit into the resonant mode path and radial mode number, n, which shows the number of maxima of the electromagnetic field in the radial direction inside the sphere. From Eq.(2.36) and Eq.(2.37) which describe the respective amplitudes of individual TM and TE modes inside the sphere, the positions of TM and TE resonances can be determined as the values of size parameter x for which the denominator of Eq.(2.36) (TM resonance) or Eq.(2.37) (TE resonance) goes to zero:

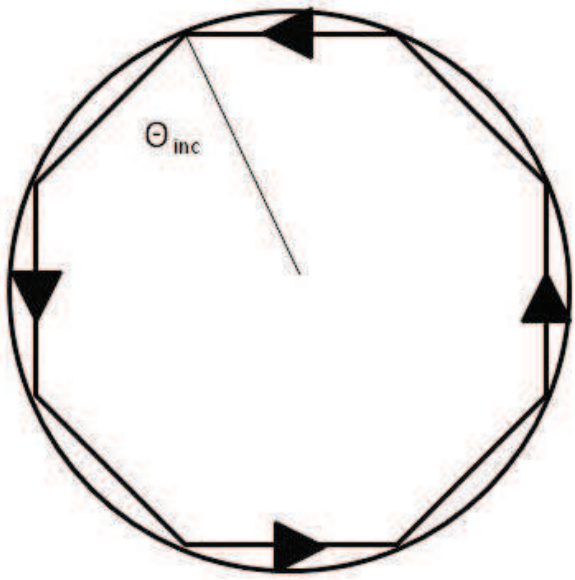

Figure 2.2: The ray at a glancing angle is fully reflected. When the optical path is equal to an integer number of wavelengths, a resonance is formed.

$$\frac{\psi_l'(\bar{n}(\omega)x)}{\psi_l(\bar{n}(\omega)x)} - \bar{n}(\omega)\frac{\xi_l^{(1)'}(x)}{\xi_l(x)} = 0 \tag{2.46}$$

$$\bar{n}(\omega)\frac{\psi_l'(\bar{n}(\omega)x)}{\psi_l(\bar{n}(\omega)x)} - \frac{\xi_l^{(1)'}(x)}{\xi_l(x)} = 0 \tag{2.47}$$

In the case there is no absorption loss in the cavity ($\bar{n}_i(\omega)$=0), the solutions of Eq.(2.46) and Eq.(2.47) are the complex resonance size parameters x_α. The real part of x_α is the position of the resonance mode and the leakage loss of the cavity is related to the imaginary part of x_α. These parameters are related to Q-factor of cavity which is [29]:

$$Q = \frac{Re(x_\alpha)}{2Im(x_\alpha)} = \frac{\omega_\alpha}{\Delta\omega_\alpha} = \omega_\alpha\tau, \tag{2.48}$$

where $\omega_\alpha = cRe(x_\alpha)/a$ and τ are the resonance frequency and the lifetime of the resonance respectively. Factors such as volume inhomogeneities, surface roughness, shape deformations, nonlinear effects and absorption are limiting and decreasing the maximum Q values to be less than 10^{10} [31].

Chapter 3

FÖRSTER RESONANCE ENERGY TRANSFER

3.1 Introduction

Luminescence is the emission of light from any substance which occurs from electronically excited states of matter. Photoluminescence exploits absorption of light for the generation of excited state and it can be formally categorized into two groups which differ by the nature of the transition from the excited state to the ground state: Fluorescence with singlet-singlet transition and phosphorescence with triplet-singlet transition. In addition to radiative relaxation of excited electronic state, the absorbed energy can be released in a number of non-radiative processes such as intramolecular charge transfer, conformational change, intersystem crossing, internal conversion, vibrational relaxation and energy transfer [32].

Energy transfer is a mechanism which provides information on immediate neighbourhood of a molecule by influencing its fluorescence spectrum, quantum yield and lifetime of fluorescence [33]. FRET is one of the relaxation mechanisms describing energy transfer between two chromophores of fluorescence dyes. Due to the high sensitivity to separation distance between the two chromophores involved in the energy transfer, FRET has found numerous applications in optical imaging and analysis of intermolecular interactions [34]. In many areas of biological research, precise location and nature of the interaction between specific molecular species within living cells has to be known. Because the transfer rate is sensitive to the distance between the two involved fluorophores, FRET is used as a molecular 'ruler' to measure the distance among biological molecules [35]. In this chapter the principles of FRET theory are presented. The absorption and emission processes of a molecule are also described.

3.2 Fluorescence

The emission of light from electronically excited states of materials is called luminescence which is categorized into two groups as fluorescence and phosphorescence. Fluorescence is the emission of the light from singlet excited state whereas the phosphorescence transition occurs from the triplet excited state. In the singlet excited state, the electron in the higher energy orbital has the opposite spin orientation compared to the second paired electron which is in the ground state energy orbital. Regarding the triplet excited state, the two electrons are unpaired (they have the same spin orientation) and, thus, it requires to change the spin orientation while the excited electrons return to ground state. Fluorescence emission occurs when electrons return from singlet excited state to the lower energy orbital and the period of time of this return is extremely short, in the range of 10^{-8} s. The phosphorescence lifetimes are longer than fluorescence lifetimes and its range varies from 10^{-3} second to a few seconds or longer [36].

Fluorescence is typically observed in aromatic substances which show molecular planarity and delocalizated electrons on multiple conjugated double bounds [37]. Hundreds of fluorescent molecules which are called fluorophores have been used for many applications such as fluorescent imaging and spectroscopy[34]. In imaging, fluorophores are used to visualize molecules such as proteins and DNA without undergoing changes of quantum yield and spectral profile. Fluorescent molecules can be also used as gain medium for dye lasers. Broad emission spectra and wide range of available fluorophores allow construction of tunable dye lasers with emission wavelengths covering the whole visible spectrum.

3.2.1 Jablonski Diagram

Jablonski diagram describes the energy levels of a molecule and possible transitions between them and it is used to illustrate various molecular processes following absorption of light by the molecule. Professor Alexander Jablonski is known as the father of fluorescence spectroscopy and Jablonski diagram is named after him [34].

In Fig. 3.1, an example Jablonski diagram is demonstrated with possible energy transitions. The singlet ground (S_0), first excited (S_1) and second excited (S_2) electronic states are shown and the fluorophores exist in a number of vibrational energy levels which correspond to 0, 1 and 2 at S_0, S_1 and S_2. The instantaneous nature of light absorption (processes

labeled $h\nu_A$) is demonstrated by transitions between states as vertical lines. Absorption of light typically leads to transitions between the lowest vibrational level of S_0 state and higher vibrational levels of S_1 state.

Following light absorption, the molecules in condensed states rapidly relax to the lowest vibrational level of S_1, which is defined as internal conversion. This process occurs on the time scale around 10^{-12} sec and this is non-radiative transition between two electronic or vibrational states [33]. Since the typical lifetimes of fluorescence are in time scales of 10^{-8} sec, internal conversion will be completed prior to the light emission. Therefore, fluorescence emission occurs from a thermally equilibrated excited state, which is, the lowest energy vibrational state of S_1.

Fig. 3.1 illustrates that radiative return to the ground electronic state occurs to a higher vibrational ground state level (processes labeled $h\nu_F$), which quickly reaches thermal equilibrium in time scales of 10^{-12} sec. Return to an excited vibrational state at the level of S_0 state causes the vibrational structure in the emission spectrum. Consequence of emission to higher vibrational ground states is that the emission spectrum is typically a mirror image of the absorption spectrum of the S_0 to S_1 transition. The reason of similarity is that electronic excitation does not change significantly the spacing of the vibrational levels [36].

In addition to fluorescence which occurs from S_1 excited state, emission from T_1 excited state known as phosphorescence can occur. This emission follows the spin-state conversion from S_1 singlet to T_1 triplet and it is shifted to longer wavelengths compared to fluorescence. This conversion from S_1 to T_1 is defined as intersystem crossing and transition from T_1 to singlet ground state is not allowed. As a result phosphorescence emission is effected by factors such as solvents and quenching which results in the rate constants for triplet emission being several orders of magnitude smaller than those for fluorescence [36].

3.3 Characteristics of Fluorescence Emission

The fluorescence emission shows several general characteristics. Fluorescence molecules have common characteristic properties described in the following section.

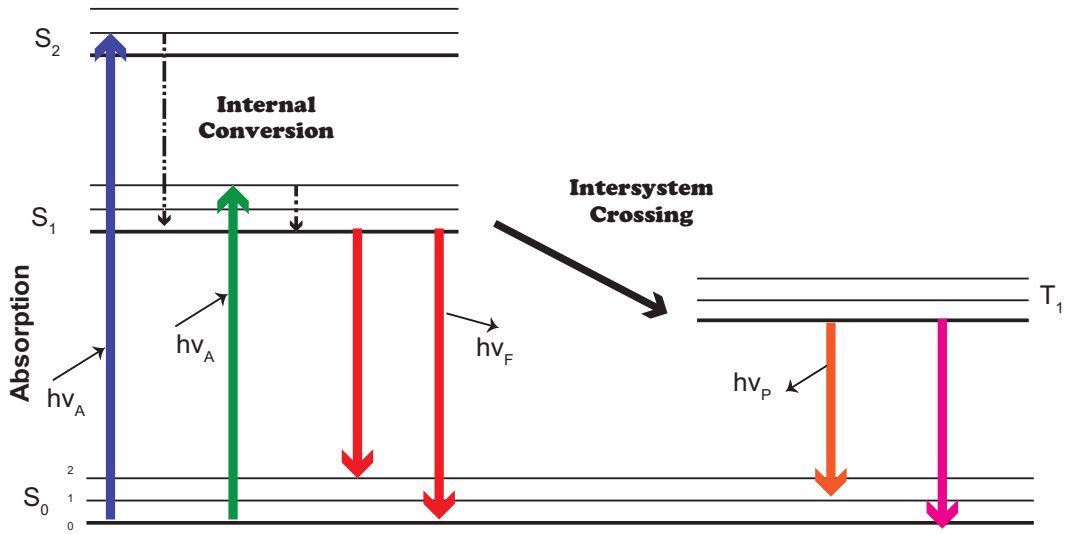

Figure 3.1: Jablonski Diagram illustrating the process of light absorption and relaxation of the excited state by fluorescence and phosphorescence.

3.3.1 The Stokes Shift

Examination of the Jablonski diagram shows that the energy of the emission is naturally less than that of absorption. The fluorescence occurs at lower energies which corresponds to longer wavelengths. Sir G. G. Stokes in 1852 at the University of Cambridge observed this phenomenon [38] which is named as Stokes Shift.

Stokes shift is the difference between positions of the band maxima of the absorption and emission spectra of the same electronic transition. When system is excited, it absorbs photons and gains energy and then emitting photons cause energy losses. The difference in energy between the absorbed photons and the emitted photons defines the Stokes shift. Energy losses are observed specifically between excitation and emission for fluorescent molecules in solution. One of the causes of the Stokes shift is the rapid decay of excited molecules to the lowest vibrational level of S_1 via internal conversion. Subsequently, fluorophores decay to higher vibrational levels of S_0 which causes loss of excitation energy by thermalization of the excess vibrational energy. Additionally, Stokes shift can be displayed

by fluorophores due to solvent effects such as energy transfer between the fluorophore and the solvent molecules [36].

3.3.2 Fluorescence Lifetimes and Quantum Yield

Fluorescence lifetime τ and quantum yield Q have the most important role to characterize a fluorophore. The number of emitted photons relative to the number of absorbed photons defines the quantum yield. The brightest emission is mostly displayed by substances with the largest quantum yields. The lifetime and quantum yield are represented in Fig. 3.2 with a basic Jablonski diagram. Here, emissive rate of the fluorophore (Γ) and its rate of non-radiative decay to S_0, (k_{nr}), are used to determine quantum yield which is given by Eq.(3.1). The quantum yield is defined as ratio between number of emitted photons and absorbed photons [34].

$$Q = \frac{\Gamma}{\Gamma + k_{nr}} \tag{3.1}$$

Due to Stokes losses, the energy yield of fluorescence is less than unity. If radiationless decay rate k_{nr} is smaller than the rate of radiative decay Γ, quantum yield could be close to unity. Briefly, the quantum yield can be between 0 and 1, where 0 corresponds to non-fluorescing materials and 1 corresponds to highly fluorescent materials, in the case that every photon absorbed results in a photon emitted.

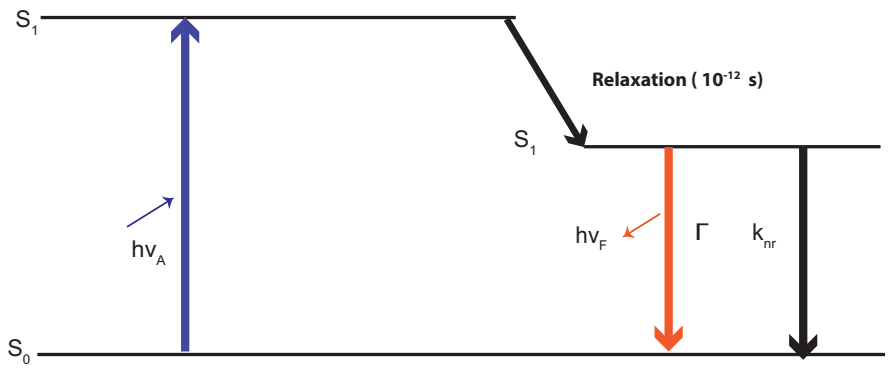

Figure 3.2: A basic Jablonski diagram illustrating the quantum yield and lifetimes

The lifetime of the excited state is the average time the molecule spends in excited state until it returns to ground state. Lifetimes range varies from 10 nsec to 10 sec and it is given by Eq. 3.2. Emission of fluorescence is a random process, only a few molecules emit their photons at $t = \tau$. Hence, an average value of the time spent in the excited state describes the lifetime.

$$\tau = \frac{1}{\Gamma + k_{nr}} \tag{3.2}$$

3.4 Förster Resonance Energy Transfer

FRET is an electrodynamic process by which energy is transferred non-radiatively via long range dipole-dipole interactions from the excited state of a donor to the ground state of an acceptor [19]. The rate of energy transfer can change with overlap integral of the emission spectrum of the donor and the absorption spectrum of the acceptor, the distance between the donor and acceptor molecules and relative orientation of the donor and acceptor transition dipoles.

FRET is used in all applications of fluorescence such as optical imaging and analysis of intermolecular interactions. FRET measurements can be utilized as an effective molecular ruler for determining distances between biomolecules labeled with feasible donor and acceptor chromophores when they are within 2 to 10 nanometers of each other. These properties allow us to design experiments which elucidate the sizes and structural properties of the sample [34].

3.4.1 Characteristics of FRET

Förster demonstrated that the rate of energy transfer of the dipole-dipole mechanism depends on the square of potential energy and, thus, it is proportional to r^{-6} where r is the distance between donor and acceptor molecules [34]. The rate of energy transfer ($k_t(r)$) from a donor to an acceptor which depends on the distance between the dipoles is given by

$$k_t(r) = \frac{1}{\tau_D}\left(\frac{R_0}{r}\right)^6 \tag{3.3}$$

where τ_D is the decay time of the donor in the absence of the acceptor and R_0 is the Förster radius. Therefore, the rate of energy transfer is equal to the reciprocal donor decay time

for r=(R_0) [33].

Förster radius can be calculated from the spectral properties of the donor and acceptor which include the quantum yield of the donor and the overlap integral (see section 3.4.2). Also, energy transfer efficiency depends on the solvent, as the nature of microenvironment can change the orientation of the donors and acceptors. For most fluorophores, Förster radius varies between 2 to 10 nm and, thus, FRET can be used as spectroscopic ruler for measuring intermolecular and intramolecular distances comparable to R_0. Conditions that change the distance between donor and acceptor molecules will influence the rate of transfer energy. In this application, in order to calculate distance between donor and acceptor, one uses the extent of energy transfer and structural information is obtained about the macromolecule [39].

Resonance energy transfer is a process that does not involve emission and reabsorption of photons. The theory of energy transfer is based on the concept of a fluorophore as an oscillating dipole, which can exchange energy with another dipole with a similar resonance frequency. Non-molecular optical properties of the sample such as the optical densities of the sample at the absorption and emission wavelengths and the geometric arrangement of the excitation and emission light paths affect the energy transfer [34]. Basic theory of resonance energy transfer will be presented in the following section.

3.4.2 Theory of Energy Transfer

In order to explain theory of resonance energy transfer, the equations should be derived from classical and quantum mechanical considerations which is quite complex. Here only final expressions will be defined which characterize physical basis of energy transfer. Fig. 3.3 shows Jablonski diagram for a combined system of donor and acceptor molecule which can exchange energy via FRET channel characterized by rate $k_t(r)$. The rate of energy transfer is given by

$$k_t(r) = \frac{\kappa^2 Q_D}{\tau_d r^6}\left(\frac{9000(ln10)}{128\pi^5 N n^4}\right)\int_0^\infty F_D(\lambda)\epsilon_A(\lambda)\lambda^4\, d\lambda \tag{3.4}$$

where Q_D is the quantum yield of the donor in the absence of acceptor, n is the refractive index of the medium, N is Avogadro number, r is the distance between the donor and acceptor, and τ_D is the lifetime of the donor in the absence of acceptor. $F_D(\lambda)$ is corrected

dimensionless spectrum of the fluorescence intensity of the donor in the wavelength range $\lambda + \delta\lambda$ with total intensity normalized to unity. $\epsilon_A(\lambda)$ is the molar extinction coefficient of the acceptor at wavelength λ. Typically, it is in units of $\mathrm{M}^{-1}\mathrm{cm}^{-1}$. κ^2 is the orientation factor in space of the transition dipoles of the donor and acceptor. Typically, it is assumed to be 2/3 which is the value for donors and acceptors that randomize by rotational diffusion prior to energy transfer. This assumption is justified in biological experiment where the fluorophores can rotate freely with a fixed distance between them. κ^2 is given by [40, 34].

$$\kappa^2 = (\cos\theta_T - 3\cos\theta_D \cos\theta_A)^2 \tag{3.5}$$

where $\cos\theta_T$ is the angle between the emission transition dipole of the donor and the transition absorption dipole of the acceptor and $\cos\theta_D$ and $\cos\theta_A$ are angles between these dipoles and the vector joining the donor and the acceptor.

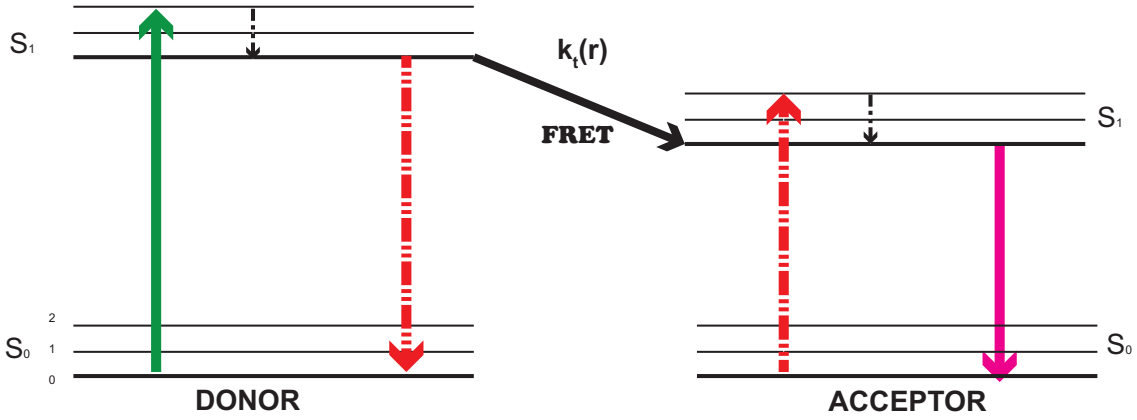

Figure 3.3: Jablonski diagram for FRET illustrating the coupled transitions between the donor emission and acceptor absorption (dashed arrows).

The fluorophores are chosen to release energy of the donor to acceptor. The spectral overlap defines this overlap between the emission spectrum of the donor and the absorption spectrum of the acceptor. The overlap integral is defined as

$$J(\lambda) = \int_0^\infty F_D(\lambda)\epsilon_A(\lambda)\lambda^4\, d\lambda \tag{3.6}$$

$\epsilon_A(\lambda)$ is defined in terms of $M^{-1}\ cm^{-1}$ and F_D is dimensionless. With λ in nanometer it follows that $J(\lambda)$ has units of $\mathrm{M}^{-1}\ \mathrm{cm}^{-1}\ \mathrm{nm}^4$ [36].

According to Eq. 3.3, the rate of energy transfer $k_t(r)$ is equal to the decay rate (τ_D^{-1}) when the distance between donor and acceptor is equal to R_0. Hence, by substituting Eq. 3.4 into Eq. 3.3 we obtain

$$R_0^6 = \frac{\kappa^2 Q_D 9000(ln10)}{128\pi^5 N n^4} J(\lambda) \tag{3.7}$$

where the Förster distance in $\mathring{A}$ is given by

$$R_0 = 0.2108[\kappa^2 n^{-4} Q_D J(\lambda)]^{1/6} \tag{3.8}$$

Here, the Förster distance is defined with assumed value of κ^2 which is 2/3. The efficiency of energy transfer (E) is defined as the fraction of excited donors transferring their energy to the acceptor. Using Eq. 3.3 for the rate of energy transfer, FRET efficiency can be expressed as

$$E = \frac{k_t(r)}{\tau_D^{-1} + k_t(r)} \tag{3.9}$$

The case when the transfer rate is faster than the inverse decay time corresponds to more efficient energy transfer ($E > 0.5$). In contrast, if the transfer rate is slower than the inverse decay time, the energy transfer competes with radiative decay which is inefficient. By substituting Eq. 3.3 into Eq. 3.9, FRET efficiency can be expressed as

$$E = \frac{R_0^6}{R_0^6 + r^6} \tag{3.10}$$

which illustrates that the energy transfer efficiency depends on distance between donor and acceptor. Alternatively, the transfer efficiency can be expressed as a function of relative fluorescence intensity of the donor in the absence of (F_D) and presence (F_{DA}) of acceptor.

$$E = 1 - \frac{F_{DA}}{F_D} \tag{3.11}$$

As function of lifetimes, it is possible to calculate transfer efficiency as

$$E = 1 - \frac{\tau_{DA}}{\tau_D} \tag{3.12}$$

where τ_{DA} and τ_D are lifetimes of the donor in the presence of acceptor and the absence of acceptor respectively.

Eq. 3.11 and Eq. 3.12 are derived from assumptions that the donor and acceptor pairs are separated by a fixed distance. A single fixed distance between donor and acceptor is not found for mixture of donors and acceptors in solution. This needs more complex expressions which can be derived by averaging the transfer rate over assumed spatial distribution of donor-acceptor pairs [41].

Chapter 4

MATHEMATICAL MODELING OF RATE EQUATIONS FOR DYE LASER

4.1 Introduction

Distributed Feedback Dye Lasers (DFDL) use periodic modulation of refractive index of the gain medium of periodic modulation of the gain itself to provide feedback mechanism for lasing [42]. Due to relaxation oscillations in the gain medium, pumping of DFDL with nanosecond pulses results in generation of 20-100 time shorter picosecond output pulses [43]. DFDL provides higher efficiency, broader wavelength tuning range and lower amplified spontaneous emission (ASE) background level compared to other mechanisms for generating ultra-short pulses. The significant pulse shortening in DFDL is caused by self Q-switching which is a result of spatial gain modulation dependence of the feedback. To have even shorter and more stable pulses, a saturable absorber can be added to distributed feedback dye medium to produce additional self Q-switching [44].

There have been many attempts to improve dye lasers efficiency and to extend their spectral range of operation. Energy transfer dye lasers (ETDL) which use energy transfer in a multi-component gain medium to achieve wider tuning range of output wavelength and higher output power at lower dye concentrations represent one of the alternatives to lasers based on a single dye. Lower pump threshold and pulse width are additional advantages of ETDL in comparison to single dye laser case. First ETDL was demonstrated in 1968 by Peterson [45] who first reported enhanced laser efficiency through using donor-acceptor pairs. Dienes developed a model of ETDL and matched theoretical results with experimental results for donor-acceptor dye pair, commonly used for ETDL studies. Using this model, the variation of gain with acceptor concentrations was demonstrated and subsequent gain measurements of donor-acceptor pair showed higher gain compared to single dye [46]. The conversion efficiency of the system was substantially increased as a result of gain enhancement where donor molecules were directly excited by a pump beam and excitation energy

was subsequently transferred from donor molecules to acceptor molecules.

In the first part of this chapter, the characteristic behavior of DFDL using a mixture of laser dye and saturable absorber is modeled theoretically by using rate equations as a first step to model properties of FRET lasing in micro-droplet cavity [44]. Subsequently, theoretical model for energy transfer distributed feedback dye laser (ETDFDL) is presented. The behaviors of ETDFDL with Rhodamine-6G (donor) and Ab7 (acceptor) dye pair as active medium is studied in terms of donor concentration and the pump power taking into account energy transfer [47].

4.2 Rate Equations for Passive Q-Switched DFDL and Simulation Results

In this section, coupled differential equations system used to determine characteristics of the DFDL which contains mixture of laser dye and saturable absorber dye is presented.

Let's define *n(t)* as the spatially averaged density of laser dye molecules in the excited level S_1 and $n_a(t)$ as the spatially averaged density of absorber dye molecules in the ground level S_0 with the units of cm^{-3}.Rate equations for the two population densities then read as [44]

$$\frac{dn(t)}{dt} = I_p(t)\sigma_p[N - n(t)] - \frac{\sigma_{ell}c}{\eta}n(t)q(t) - \frac{n(t)}{\tau} \tag{4.1}$$

$$\begin{aligned}\frac{dn_a(t)}{dt} = -I_p(t)\sigma_{pa}n_a(t) + \frac{\sigma_{eal}c}{\eta}[N_a - n_a(t)]q(t) + \frac{N_a - n_a(t)}{\tau_a} - \frac{\sigma_{aal}c}{\eta}n_a(t)q(t) \\ + \frac{2\Omega_a}{\tau_a L(\sigma_{eaa} - \sigma_{1aa})}(exp((\sigma_{eaa} - \sigma_{1aa})[N_a - n_a(t)]L) - 1)\end{aligned} \tag{4.2}$$

where N and N_a are the total density of laser and absorber dye molecules, values of cross sections of the laser dye and saturable absorber are given in Table 4.1, and all the remaining parameters are summarized in Table 4.2. The first three terms of the right-hand side of Eq.(4.2) are analogous to the three terms of Eq.(4.1) and correspond to pump light absorption, stimulated emission, and spontaneous emission rates, respectively. The fourth term of Eq.(4.2) describes the decrease of the ground-state absorber molecules which is caused by the absorption of lasing photons emitted from the laser dye [44]. The last term of Eq.(4.2) is a significant term in rate equation and describes the decrease in the excited-state density of the absorber molecules which means the increase in the absorber ground state

Table 4.1: Cross Sections of Laser Dye (Coumarin 153) and Saturable Absorber (Rhodamine B)

Symbols	Meaning of the symbol	Numerical Value
σ_p	Absorption Cross-section of Laser Dye at the Pumping Wavelength	$1.15 \times 10^{-17}\ cm^2$
σ_{pa}	Absorption Cross-section of Absorber Dye at the Pumping Wavelength	$3.8 \times 10^{-17}\ cm^2$
σ_{ell}	Emission Cross-section of Laser Dye on Lasing Wavelength (λ_1)	$1.1 \times 10^{-16}\ cm^2$
σ_{1ll}	Excited-state Absorption Cross-section of the Laser Dye on Lasing Wavelength (λ_1)	$0.4 \times 10^{-16}\ cm^2$
σ_{aal}	Ground-state Absorption Cross-section of the Absorber Dye on Lasing Wavelength (λ_1)	$4.1 \times 10^{-16}\ cm^2$
σ_{eal}	Emission Cross-section of the Absorber Dye on Lasing Wavelength (λ_1)	$0.9 \times 10^{-16}\ cm^2$
σ_{1al}	Excited-state Absorption Cross-section of the Absorber Dye on Lasing Wavelength (λ_1)	$1.3 \times 10^{-16}\ cm^2$
σ_{eaa}	Emission Cross-section of the Absorber Dye on (λ_a=640 nm)	$3.05 \times 10^{-16}\ cm^2$
σ_{1aa}	Excited-state Absorption Cross-section of the Absorber Dye on (λ_a=640 nm)	$2.0 \times 10^{-16}\ cm^2$

population. This term describes Amplified Spontaneous Emission (ASE) emitted by the excited absorber molecules which cause decrease in the excited state density of absorber molecules.

If we assume zero cavity feedback for absorber dye photons, situation in the DFDL cavity is completely characterized by the density *q(t)* of laser dye photons at λ_1=555 nm:

$$\begin{aligned}\frac{dq(t)}{dt} = \frac{(\sigma_{ell} - \sigma_{1ll})c}{\eta} n(t)q(t) - \frac{q(t)}{\tau_c(t)} - \frac{\Omega n(t)}{\tau} - \frac{\sigma_{aal}c}{\eta} n_a(t)q(t) \\ + \frac{\sigma_{eal}c}{\eta}[N_a - n_a(t)]q(t) - \frac{\sigma_{lal}c}{\eta}[N_a - n_a(t)]q(t)\end{aligned} \tag{4.3}$$

where τ_c is defined as equivalent cavity decay time of lasing photons at 555 nm

$$\tau_c(t) = max\left(\frac{\eta L^3}{8c\pi^2}[n(t)(\sigma_{ell} - \sigma_{1ll})V]^2, \frac{nL}{10c}\right) \tag{4.4}$$

with remaining the parameters given in Table 4.2.

Table 4.2: Meaning of the Symbols and Values of the Constants in Rate Equations

Symbols	Meaning of the symbol	Numerical Value
τ and τ_a	Decay Time of Laser and Absorber S_1 state	4.0 and 4.0 ns
L	Length of excited region	0.3 cm
c	Speed of Light	3×10^{10} cm s^{-1}
η	Refractive Index	1.32
V	Visibility of interference pattern	0.38
b	Height of the excited volume	0.02 cm
Ω	Factor determining the fraction of the spontaneous emitted photons by excited laser	5.2×10^{-8}
Ω_a	Factor determining the fraction of the spontaneous emitted photons by absorber dye molecules.	2.5×10^{-6}

In the simulations, giving a lower limit for τ_c, makes it possible to use initial values of *n(0)=q(0)*=[N_a - $n_a(0)$]=0. This lower limit reflects the fact that, due to the finite length of DFDL, the laser photons stay for finite time in the excited volume. Subsequently, the exact value of this limit changes in time, however, the solution of coupled differential equations is independent of this limit, if τ_c exceeds its value before build-up of the laser pulse. In the calculation, τ_c was higher than 100 ps before the appearance of the pulse, meanwhile the lower limit was about 1.5 ps [43].

The output power from DFDL is calculated as

$$P_{out}(t) = \frac{hcq(t)Lab}{2\lambda_1\tau_c(t)} \tag{4.5}$$

where $a = (N\sigma_p + N_a\sigma_{pa})^{-1}$ is defined as penetration depth of the pump beam into dye solution.

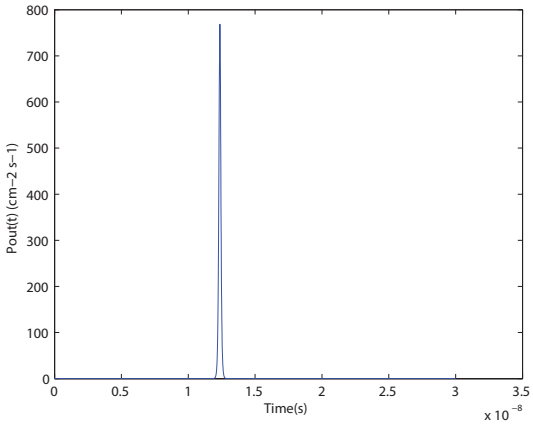

Figure 4.1: Calculated time profile of the first DFDL pulse without saturable absorber ($N_a = 0$). Pump pulse width: 9 ns

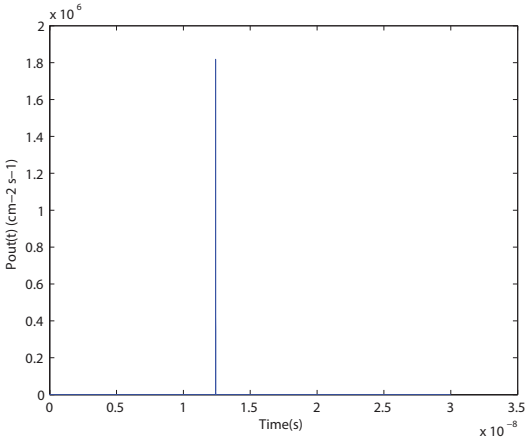

Figure 4.2: Calculated time profile of the first DFDL pulse with saturable absorber ($N_a = 6 \times 10^6$ cm^{-3}). Pump pulse width: 9 ns

Coupled differential equations Eq.(4.1)-Eq.(4.3) together with Eq.(4.4) were solved numerically. As a result of relaxation oscillation, the DFDL emits many pulses upon excitation with a single pump pulse.

Output power of the first DFDL pulse pumped with 9 ns excitation pulse is shown in Fig. 4.1 without saturable absorber in the gain medium (i.e. $N_a = 0$) and in Fig. 4.2 with saturable absorber in the gain medium ($N_a = 6 \times 10^6$ cm^{-3}) . The presence of saturable absorber causes massive increase in the output power compared to the case when only the laser dye is present in the gain medium. In calculating the effect of saturable absorber on the power and width of the output pulse energy transfer between the laser dye and absorber is ignored.

Fig. 4.3 illustrates time profile of the DFDL output pulse for different values of the pump power. As can be seen in the figure, the width of the output pulse decreases and its intensity increases when the pump power approaches lasing threshold.

4.3 Rate Equations for ETDFDL and Simulation Results

There are different mechanisms of energy transfer between donor and acceptor: radiative transfer where acceptor molecules absorb the emission by donor molecules and non-radiative

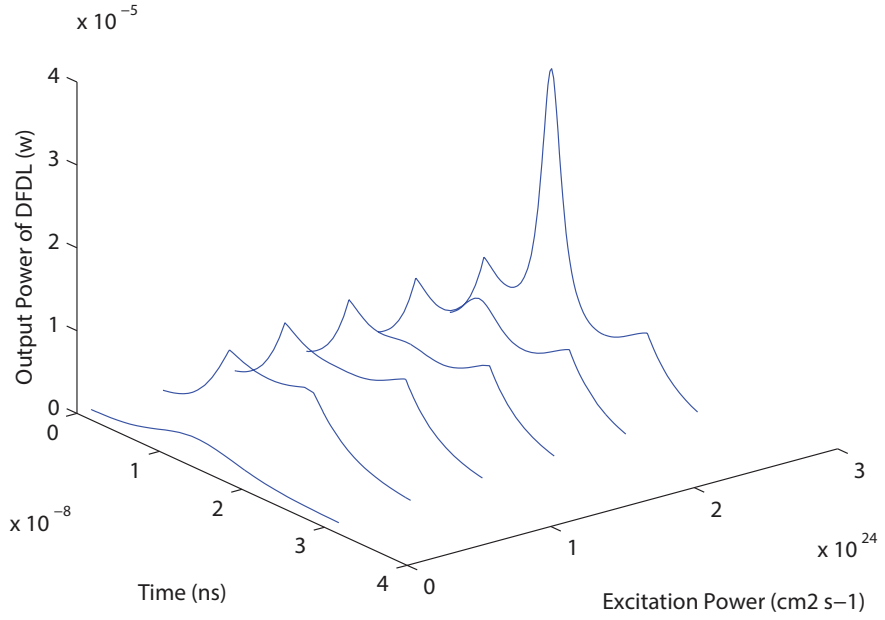

Figure 4.3: Dependence of the time profile of DFDL output laser pulse on the excitation power

resonance transfer due to long-range dipole-dipole interaction (FRET). Consequently, the rate equations have to be modified by considering appropriate mechanisms of energy transfer. If the emission spectrum of the donor and the absorption spectrum of the acceptor are overlapping, this can provide both radiative and non-radiative energy transfer between donor and acceptor. In our simulations, the rate equations have been modified by including non-radiative energy transfer (FRET) characterized by rate $(k_F)(cm^3 s^{-1})$.

The modified rate equations are similar to [43] and describe the behavior of the ETDFDL with donor and acceptor molecules. The rate of change of the density n_d of donor dye molecules in the upper (S_1) level is

$$\frac{dn_d}{dt} = I_p(t)\sigma_{pd}[N_d - n_d(t)] - \frac{\sigma_{edl} c n_d(t) q_d(t)}{n} - \frac{n_d(t)}{\tau_d} - k_F \tag{4.6}$$

where the first three terms of Eq.(4.6) denote the stimulated absorption, stimulated emission and spontaneous emission rates of donor molecules and the last term accounts for FRET to the acceptor. The rate of change of donor photon density is described by

$$\frac{dq_d}{dt} = \frac{\sigma_{edl} c n_d(t) q_d(t)}{n} - \frac{q_d(t)}{\tau_c(t)} + \frac{\Omega_d n_d(t)}{\tau_d} - \frac{\sigma_{aal} c[N_a - n_a(t)] q_d(t)}{n} - \frac{\sigma_{eal} c n_a(t) q_d(t)}{n} \tag{4.7}$$

where the first term indicates the increase of the photon density by stimulated emission and the second term expresses loss of photons in the cavity. The third and fourth term express the rate with which spontaneous emission is added to laser emission and loss of donor ETDFDL photons due to acceptor absorption, respectively. The fifth term denotes the stimulated emission rate of acceptor molecules stimulated by the donor photons. The self and passive Q-switching of ETDFDL are described by second and fourth terms, respectively.

The rate of change of acceptor molecules in the upper (S_1) level and the rate of change of acceptor photon density within laser cavity are described by

$$\frac{dn_a}{dt} = I_p(t)\sigma_{pa}[N_a - n_a(t)] - \frac{\sigma_{eaa} c n_a(t) q_a(t)}{n} - \frac{n_a(t)}{\tau_a} + \frac{\sigma_{aal} c[N_a - n_a(t)] q_d(t)}{n} - \frac{\sigma_{eal} c n_a(t) q_d(t)}{n} + k_F \tag{4.8}$$

$$\frac{dq_a}{dt} = \frac{\sigma_{eaa} c n_a(t) q_a(t)}{n} - \frac{q_a(t)}{\tau_c(t)} + \frac{\Omega_a n_a(t)}{\tau_a} \tag{4.9}$$

Meaning of the first three terms of Eq.(4.8) and Eq.(4.9) is similar as that of Eq.(4.6) and Eq.(4.7). In addition, the fourth term of Eq.(4.8) denotes the rate of increase of excited acceptor density due to the absorption of donor photons and the fifth term characterizes the rate of decrease of excited acceptor density due to the emission stimulated by the donor photons. The cavity decay time in units of (s) in given by [44]

$$\tau_c(t) = max\left(\frac{nL^3[n_d(t)\sigma_{edl}V]^2}{8c\pi^2}, \frac{nL}{10c}\right) \tag{4.10}$$

Similar to [44], the above equation is given a lower limit, which makes it possible to use the initial values $n_d(0) = 0$, $q_d(0) = 0$, $n_a(0) = 0$, $q_a(0) = 0$. The lower limit shows that fact because of finite length of ETDFDL, the laser photons can exist finite time in the excited time.

The output power of end of the ETDFDL for donor can be expressed by

$$P_{out}(t) = \frac{hcq_d(t)Lab}{2\lambda_l \tau_c(t)} \tag{4.11}$$

The output power of end of the ETDFDL for acceptor can be expressed by

$$P_{out}(t) = \frac{hcq_a(t)Lab}{2\lambda_a\tau_c(t)} \tag{4.12}$$

where $a = \frac{1}{N_d\sigma_{pd}+N_a\sigma_{pa}}$ is the penetration depth to equalize the number of incident and absorbed pump photons, and λ_1=560 nm and λ_a=650 nm are donor lasing wavelength and acceptor lasing wavelength [47].

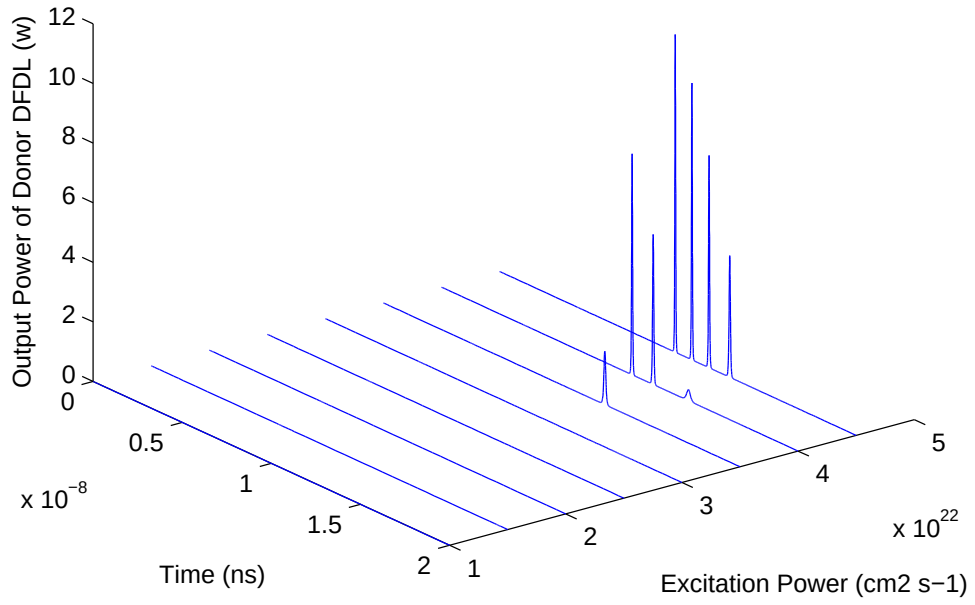

Figure 4.4: Variation of pulse width and peak output power of donor ETDFDL for different excitation power. Donor concentration is 3.0×10^{18} cm^{-3} and acceptor concentration 2.5×10^{18} cm^{-3}.

In our simulations, the donor dye molecules (Rhodamine 6G) emitting in wavelength range 545-640 nm with its peak around 560 nm and the acceptor dye molecules (Ab7) emitting in wavelength range 610-675 nm with its peak around 655 nm are chosen as the gain medium with pump source at 532 nm and 9 ns pulse width. The behavior of ETDFDL emission is studied at donor and acceptor wavelength by varying pump power and donor and acceptor concentrations. Matlab codes provided in Appendix A have been used to solve

Eq.(4.6)-Eq.(4.12) numerically and calculate the ETDFDL output power as a function of the pump power, using parameters given in [47].

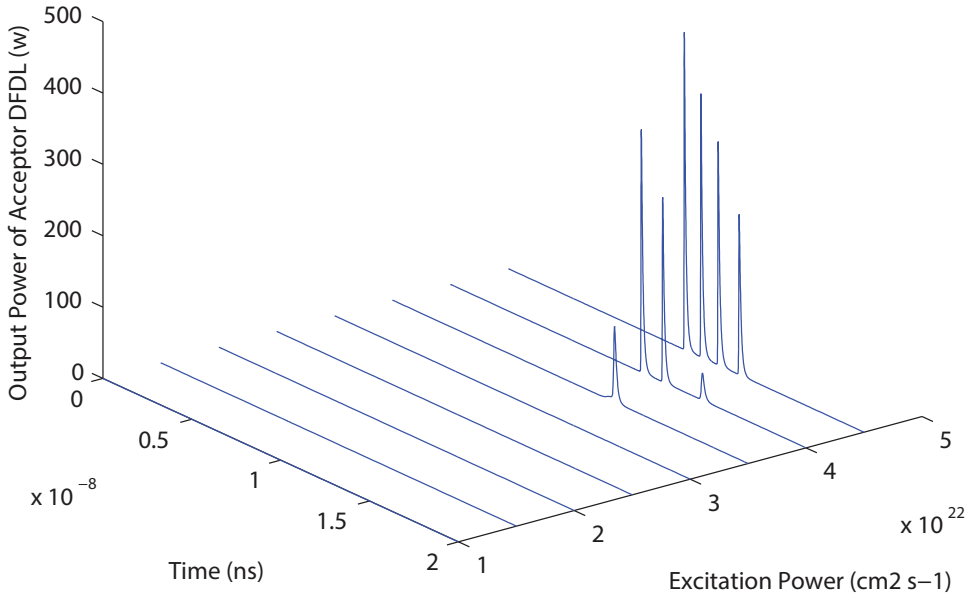

Figure 4.5: Variation of pulse width and peak output power of acceptor ETDFDL for different excitation power. Donor concentration is $3.0 \times 10^{18} cm^{-3}$ and acceptor concentration $2.5 \times 10^{18} cm^{-3}$.

First, the behavior of donor and acceptor lasing at their emission peak are studied as function of pump power. The lasing threshold is defined as minimum pump power required for the observation of lasing emission. Initially, when the pump power is below the lasing threshold, single output pulse is obtained (see Fig. 4.4). Due to faster build-up of population inversion with increase of pump rate, output power of ETDFDL single pulse increases, accompanied by decrease in pulse width. At higher pump powers above the threshold, the number of pulses emitted per a single pump pulse increases. This is valid at both donor emission peak and acceptor emission peak as shown in Fig. 4.4 and Fig. 4.5.

In Fig. 4.6, threshold analysis is carried out. According to simulations, train of pulses are emitted by ETDFDL if the pump power exceeds the threshold. Above the threshold power in the dynamic range, a single pulse is emitted by DFDL and increase in the pump

power cause the increase in the emitted pulse as shown in Fig. 4.4 and Fig. 4.5.

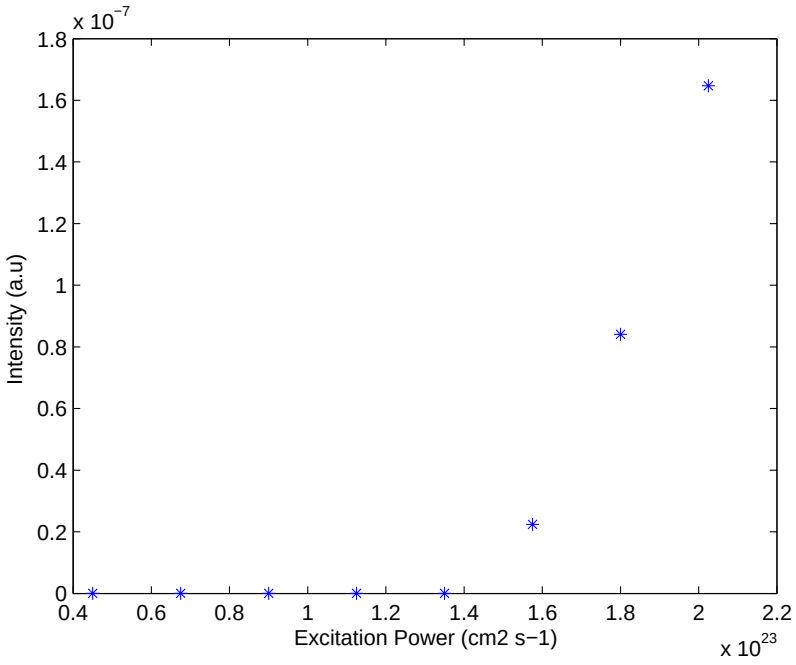

Figure 4.6: Integrated acceptor emission intensity vs. excitation power for the lasing of ETDFDL

As indication of the energy transfer lasing mechanism in ETDFDL, Fig. 4.7 provides the analysis of threshold value of acceptor lasing with a constant acceptor and varying donor concentrations. In Fig. 4.7 pump threshold fluences of acceptor lasing are shown for ETDFDL with a constant acceptor concentration of 0.5 mM and donor concentration increasing from 0 mM to 2 mM. Lasing threshold value of the acceptor decreases gradually for ETDFDL when donor concentration increases from 0 mM to 2 mM.

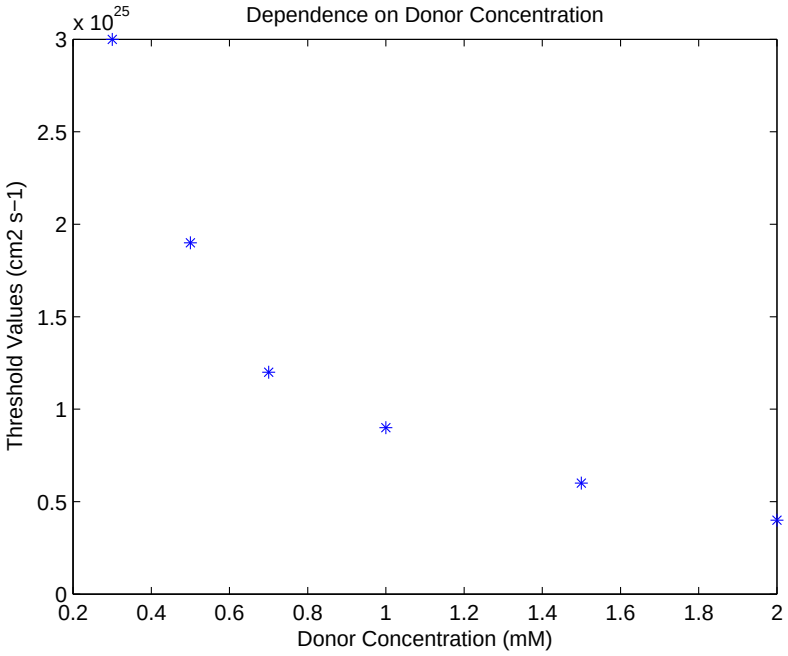

Figure 4.7: Threshold powers of acceptor lasing in ETDFDL for constant acceptor concentration of 0.5 mM, and variable donor concentration from 0 to 2 mM

Chapter 5

RESULTS AND DISCUSSIONS

5.1 Superhydrophobic Surface Preparation

Superhydrophobic surfaces are extremely water-repellent and the contact angles of aqueous droplet exceeds 150°. Glycerol/water/ethylene glycol droplets deposited on such surfaces take the shape of a truncated sphere suitable for optofluidic lasing experiments described in this thesis. The preparation of superhydrophobic surfaces is based on spin coating 50 mg/ml ethanol dispersion of hydrophobically coated silica nanoparticles (Aeroxide LE1; Degussa AG) on cover glasses [12]. The average size of these silica nanoparticles was between 7 nm and 20 nm. After procedure of spin-coating, the coated-cover glasses were dried at 85°C for half of an hour in order to vaporize remained ethanol. These superhydrophobic surfaces are transparent to visible light [48]. To deposit micron-sized droplets on these surfaces, aerosols of the droplet liquid containing the donor and acceptor dyes were generated using a compact ultrasonic nebulizer (JIH50, Beuer) and sprayed over the surface. We used glycerol/water/ethylene glycol droplets whose average contact angle measured with millimeter-sized droplets was larger than 155° on these coated-surfaces. Owing to Gibbs contact line tension [49, 30], the average contact angle of microdroplets is expected to be 1-2 degree smaller than that of millimeter sized droplets.

5.2 Experimental Setup

Experimental setup employed in our FRET lasing studies was built around an inverted optical microscope, as described in Fig.5.1. Frequency-doubled 532 nm green beam output of a home-built, passively Q-switched Nd-YVO_4 laser (20 ns pulse width and 33 kHz repetition rate) was used for optical pumping of microdroplets. After being reflected from a dichroic mirror, the pump laser beam was sent through a water-immersion objective with high numerical aperture (Nikon 60x, NA=1.2) and focused at the rim of fluorescently-stained microdroplets deposited on a cover glass with superhydrophobic coating. A relatively large

focal spot with 1.6 μm diameter was employed for the excitation beam in order to reduce sensitivity of the observed spectra to the precise position of the excitation beam with respect to the microdroplet.

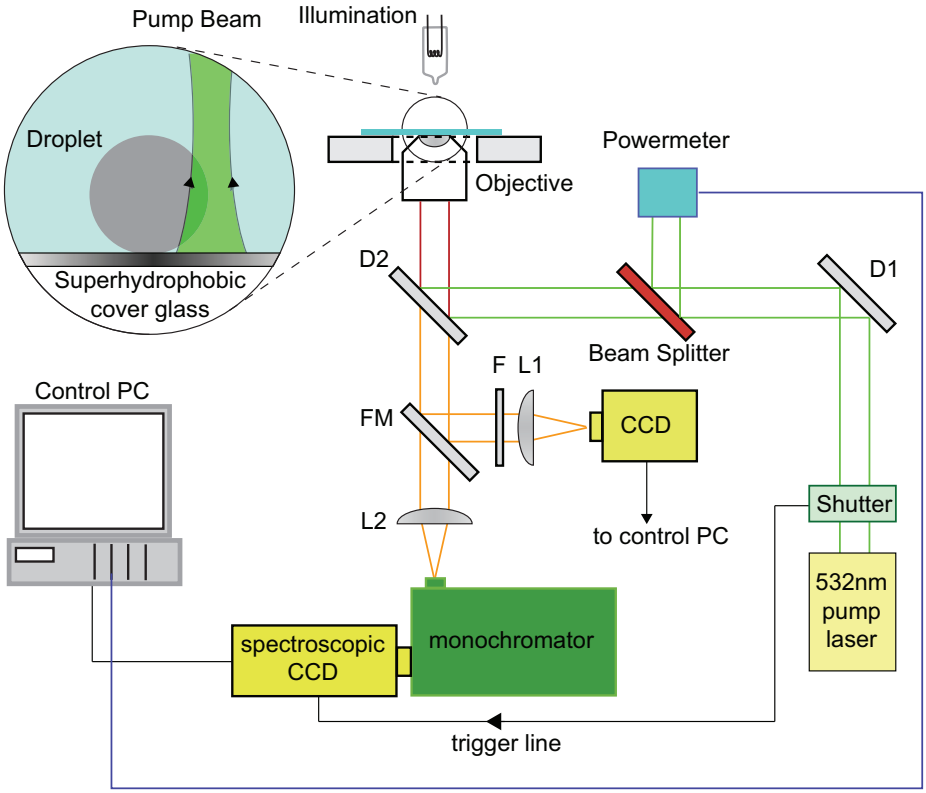

Figure 5.1: Experimental Setup for microdroplet lasing studies. The inset shows the droplet with the pump laser beam positioned on the droplet rim. D1, D2: Dichroic mirrors, F: Band-pass filter, FM: Flippable mirror, L1,L2: Lenses

Fluorescence emission of microdroplets was collected by the same microscope objective, transmitted through the dichroic mirror, and dispersed by a monochromator (focal length 500 mm; Acton Research) on the chip of a cooled CCD detector (Pixis 100; Princeton Instruments). A shutter was added to the pump laser beam path to prevent fast photobleaching of the dye molecules in the microdroplets. This shutter was only opened during the spectrum acquisition time and provided trigger signal for the CCD detector to synchronize the data recording. A polarizing beam splitter together with a half wave plate was used to control

the green beam pump power. Microdroplets were imaged with an independent CCD camera placed at the other exit port of the microscope.

5.3 Sample Preparation

Rhodamine 6G (R6G; Sigma-Aldrich) and Rhodamine 700 (R700; Radiant Dyes) fluorescent dyes were chosen as the donor and acceptor molecules for FRET during our experiments. Due to low solubility of R700 in water, we dissolved the dyes in ethylene glycol (EG) instead of water. R6G and R700 have their respective absorption peaks at 533 nm and 652 nm and respective emission peaks at 560 nm and 680 nm, thus providing a good spectral overlap for non-radiative energy transfer as can be seen in Fig. 5.2. R6G absorption profile is also well-matched for excitation with the green pump beam at 532 nm.

For the systematic characterization of FRET efficiency and determination of Förster radius of the dye pair, selected dyes have to be soluble in the used droplet liquid up to the concentrations from 0.1 mM to 2 mM. In addition, generated droplets should remain spherical and maintain a high contact angle during the experiment. EG was used as the solvent for R6G and R700 to increase dye solubility. Since EG is less polar than glycerol and water, it was possible to prepare dye solutions with concentrations as high as 2.5 mM.

Nonetheless, upon deposition of EG droplets on the surface, we observed the droplets deliberately wetted the surface and their contact angle decreased with time. This was in contrast with the behavior of droplets of glycerol/water mixture which were able to preserve their high contact angles during prolonged periods of time. To increase the stability of the droplet contact angle, 35% w/w glycerol/water was added to EG in 1 to 9 volume ratio. Resulting droplets could then preserve their spherical geometry for periods of time that were significantly longer than those of pure EG droplets and they maintained contact angles between $150° - 160°$, as determined by direct imaging of millimeter-sized droplets. Droplets prepared with this final mixture containing water, EG, and glycerol were observed to slowly evaporate during the experiments, as they were exposed to the ambient atmosphere with approximately 50 % relative humidity at room temperature. In order to minimize the uncertainty in dye concentrations caused by droplet evaporation, all the experiments reported in this thesis were performed during approximately the first 10 minutes after the droplet generation. During this time, reduction of the droplet size was measured to be less

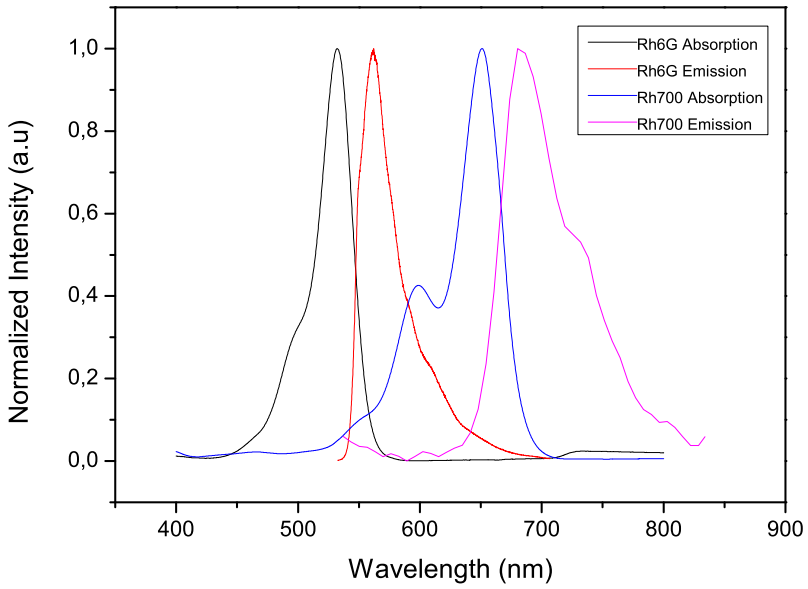

Figure 5.2: The spectrum for emission and absorption of Rhodamine 6G and Rhodamine 700 dissolved in ethylene glycol

than 7 % which corresponds to the maximal increase of the dye concentrations of $\sim 20\,\%$ with respect to the initial values. We point out that all dye concentrations reported in this thesis refer to those in the initial solutions used for droplet generation [50].

5.4 Förster Radius and FRET Efficiency Calculation

In the intensity-based FRET characterization method, FRET efficiency and Förster Radius are determined by changing acceptor concentration under constant donor concentration. During FRET, the amount of emitted photons from the donor fluorophore decreases and the emission intensity from the acceptor fluorophore increases. The FRET efficiency is basically calculated from the ratio of emission intensities from donor and acceptor before and after FRET occurrence [40].

First, the emission spectra were recorded and analyzed from bulk EG solutions with varying acceptor and donor concentrations (see Fig. 5.3) to calculate the energy transfer efficiency and Förster radius of the R6G/R700 FRET pair. EG solutions of dyes were enclosed into thin sample cells obtained by attaching two cover glasses to each other with

double sided tape and fluorescence was excited by $\lambda = 532$ nm CW laser light with 5 mW output power for these measurements.

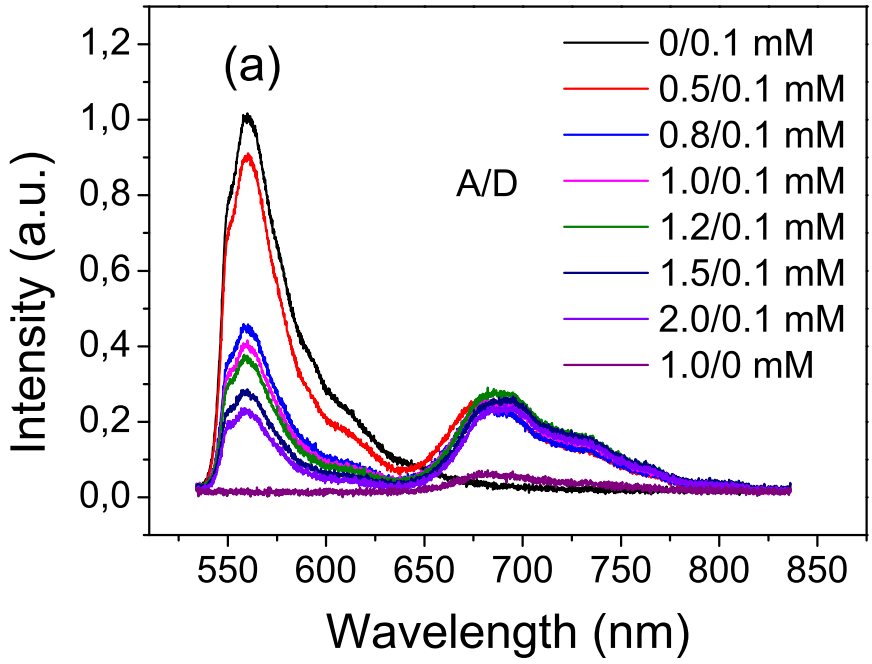

Figure 5.3: (a) Bulk fluorescence spectra recorded from mixture of R700/R6G dyes in solution for different concentration combinations A/D. All spectra were acquired with constant excitation by a 5 mW CW, 532 nm laser. The spectra were collected for a constant donor concentration of 0.1 mM and acceptor concentration changing from 0 mM to 2.0 mM. "A/D = 1.0/0 mM" for 1.0 mM acceptor in the absence of donor was recorded as well.

In Fig. 5.3, the solution of 1 mM R700 shows negligible emission in the absence of R6G because the pump wavelength is not at the same region with the absorption band of R700. On the other hand, highest intensity of R6G emission is observed for the solution containing 0.1 mM R6G and no R700 in which FRET does not exist. As the R700 concentration is gradually increased in the presence of 0.1 mM R6G, the acceptor emission shows up with a peak around 690 nm and the donor intensity is suppressed due to the FRET mechanism. Fig. 5.4 illustrates the energy transfer efficiency for each studied acceptor to donor ratio (A/D) obtained by:

$$E = 1 - \frac{F_{DA}}{F_D}, \tag{5.1}$$

where F_{DA} and F_D are the donor emission intensity in the presence and absence of the

acceptor, respectively.

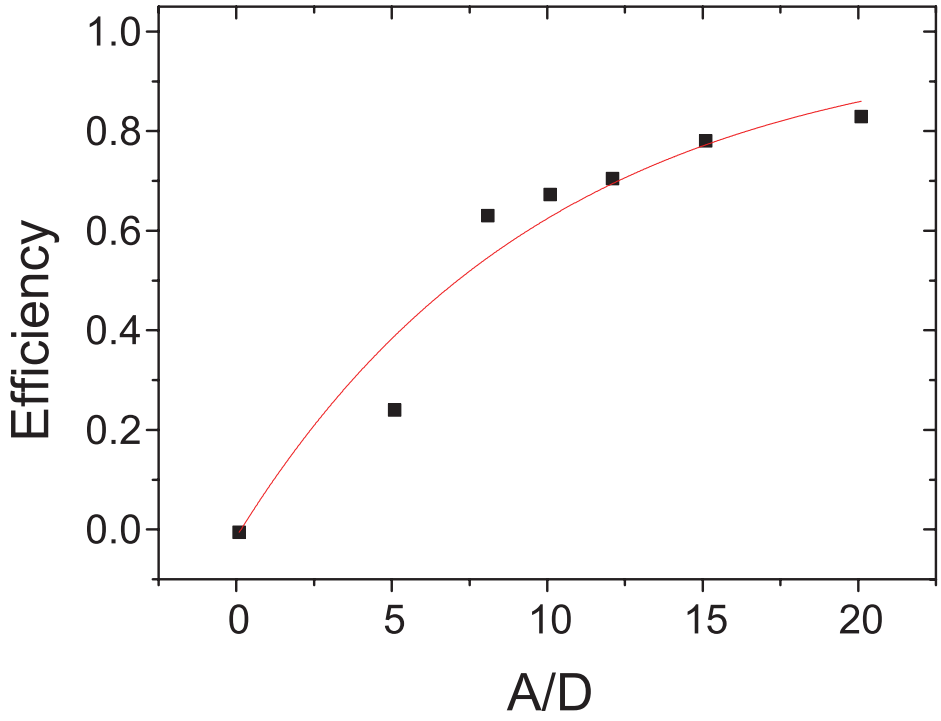

Figure 5.4: Energy transfer efficiency between R6G and R700 dyes calculated from the spectra presented in Fig. 5.3 and Eq. 5.1 (black squares). Red curve represents the fit of the experimental data points with Eq. 5.2.

For each studied value of A/D, donor emission intensity was calculated by integrating the overall emission spectrum between 535 nm and 650 nm to find out difference of emission intensity. According to [19], E is described in terms of the acceptor concentration, c, by the following equation:

$$E = \exp(-1.42c/c_0), \tag{5.2}$$

where c_0 is a reference concentration which is called the critical transfer concentration. c_0 corresponds to an average of one acceptor molecule in a sphere of radius R_0, where the Förster radius R_0 is the critical distance for which non-radiative energy transfer rate from donor to acceptor and spontaneous emission rate of the donor are equal. Förster radius can be found from c_0 by:

$$R_0 = \left(\frac{3}{4\pi \mathrm{N} c_0}\right)^{1/3}, \tag{5.3}$$

where N is the Avogadro number ($6.023 \times 10^{23}\,\mathrm{mol}^{-1}$) and c_0 is in the units of M (mol/L). By fitting Eq. 5.2 to the experimental data of Fig. 5.4, we found $c_0 = (1.41 \pm 0.13)$ mM and $R_0 = (6.6 \pm 0.2)$ nm. R_0 represents a characteristic parameter of every dye pair defining the distance at which the efficiency is 50%. For R6G/R700 dye pair, energy transfer efficiency becomes 50% when the acceptors concentration is 0.69 mM (A/D=6.9) which represents a highly efficient energy transfer between the donor and acceptor [6].

5.5 FRET Lasing in Droplets

After characterizing energy transfer in the bulk R700/R6G solutions we carried out experiments with R700/R6G doped EG/glycerol/water microdroplets standing on a superhydrophobic surface to observe FRET in a cavity.

Figure 5.5 and Figure 5.6 demonstrate lasing in the donor emission region for a droplet containing only donor and a series of FRET lasing spectra recorded from droplets with a constant donor concentration of 0.1 mM and acceptor concentration varying between 0.5 mM and 2 mM, respectively. For all spectra shown in the two figures, the excitation fluence was equal to 74 mJ/cm^2. The droplets which were generated by the ultrasonic nebulizer had an initial large size distribution ranging from a few up to $\sim$50 μm in diameter, but only droplets with diameters between 16-19 μm were chosen for the analysis to minimize the uncertainty in the lasing properties caused by the microdroplet size variations [50].

As shown in Fig. 5.5, in the absence of R700 acceptor dye, lasing from droplets containing 0.1 mM R6G is observed in the spectral region around 600 nm. Threshold analysis carried out as described in [14] and presented in the inset of Fig. 5.5 reveals threshold fluences around 7.3 mJ/cm^2 for WGMs located in the donor emission region.

In contrast, when acceptor is added to the droplet liquid, no lasing in the donor spectral region is observed with the pump fluence of 74 mJ/cm^2. Instead, broadband donor emission intensity shown in Fig. 5.6 declines with increasing acceptor concentration while the corresponding changes in the background and lasing emission of the acceptor are negligible. In all of the spectra presented in Fig. 5.6, the excitation laser fluence was 74 mJ/cm^2. At this excitation fluence, lasing modes of droplets containing both dyes appear solely in the

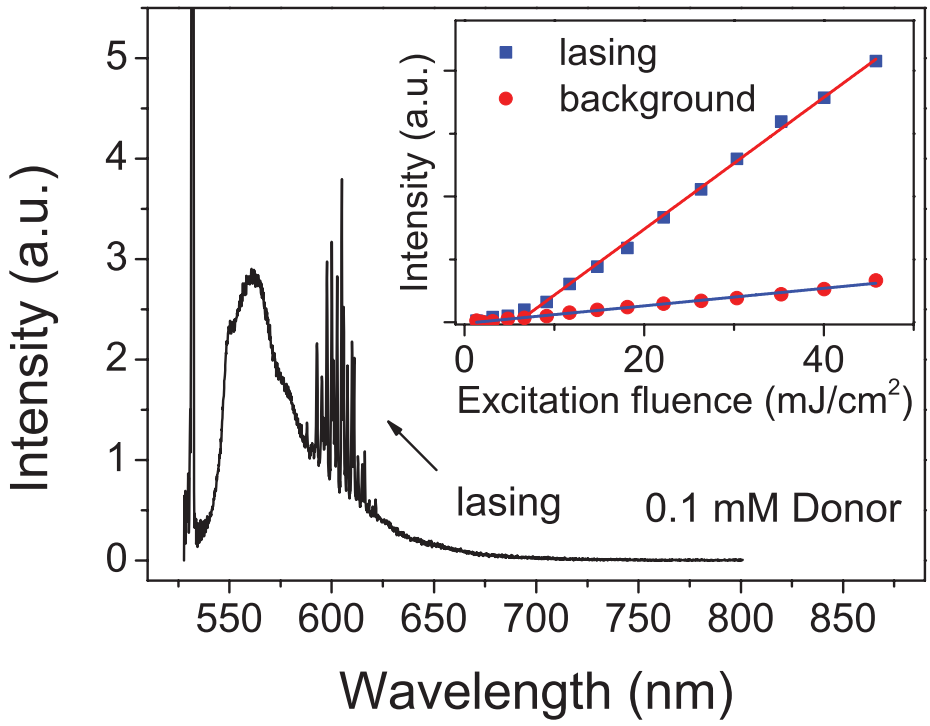

Figure 5.5: Lasing peaks of the donor emission around 600 nm for a microdroplet containing 0.1 mM R6G and no R700 at 74 mJ/cm^2 excitation laser fluence. Inset illustrates determination of the pump threshold fluence from the dependence of the WGM emission intensity on the pump beam fluence.

acceptor emission region between 740-800 nm. Donor lasing is observed only from droplets without acceptors, with lasing peaks around 600 nm. As acceptor was added to donor-doped droplets, lasing peaks shifted to 750 nm which corresponds to acceptor emission. Again, as the acceptor concentration is increased, donor intensity is suppressed similar to bulk measurement in Fig. 5.3. In spite of the low pump threshold for donor lasing from droplets which only contain R6G, donor lasing is completely suppressed by increasing acceptor concentrations due to the FRET mechanism even at a high excitation fluence of 74 mJ/cm^2 [50].

Another indication of FRET lasing mechanism in microdroplets is shown by comparing threshold pump fluence of acceptor lasing with changing donor concentration and a constant acceptor concentration. In Fig. 5.7 we demonstrate the average pump threshold fluences of acceptor lasing for microdroplets with a constant acceptor concentration of 0.1 mM and donor concentration increasing from 0 mM to 2 mM. 10 microdroplets with diameters be-

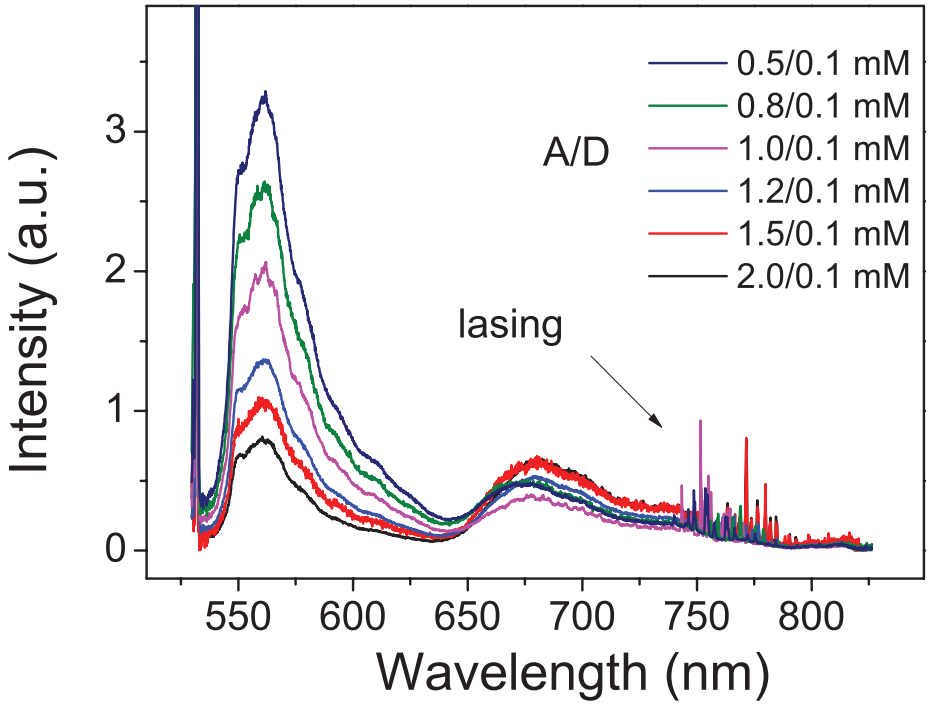

Figure 5.6: FRET lasing spectra from R700/R6G doped microdroplets with diameters between 16-19 μm situated on a superhydrophobic surface. For all spectral recordings, excitation laser fluence was 74 mJ/cm^2. R6G concentration was at 0.1 mM and R700 concentration was varied from 0.5 mM to 2 mM.

tween 16-19 μm were analyzed for each donor concentration and the error bars indicate the standard deviation of threshold fluences of acceptor lasing determined from these 10 measurements [50]. Average lasing threshold fluence of the acceptor decreases from 126 mJ/cm^2 for droplets with no donor to 6.3 mJ/cm^2 for those containing donor at 2 mM concentration.

In Fig. 5.8 emission spectra in the acceptor lasing region are shown for three droplets of similar size ($\sim$18 μm diameter) which were excited using the same excitation fluence of 16 mJ/cm^2. These microdroplets have the same R700 concentration of 0.1 mM and different R6G concentrations of 0.1 mM, 0.5 mM, and 1.0 mM.

For the droplet containing 0.1 mM R6G, acceptor lasing is not observed at the given pump laser fluence. When R6G concentration is increased to 0.5 mM, acceptor lasing is observed with relatively low intensity as the pump fluence is only slightly above the lasing threshold for this particular donor concentration. However, intense acceptor lasing appears clearly for the droplet containing 1.0 mM R6G as the pump fluence is well above the lasing

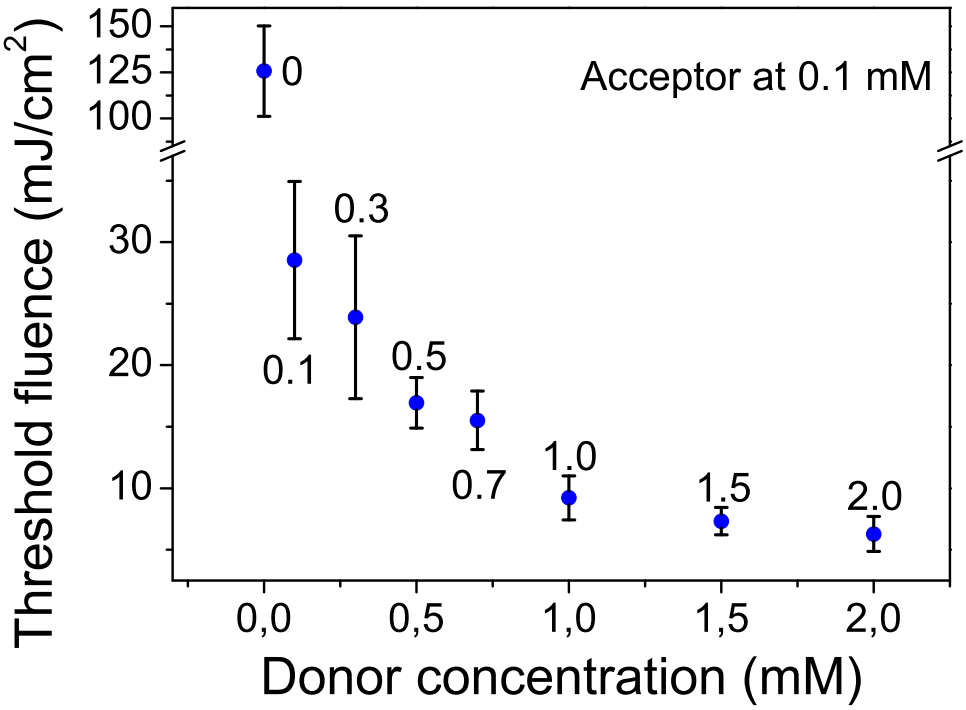

Figure 5.7: Average threshold fluences of acceptor lasing for droplets with 16-19 μm diameter, constant acceptor concentration of 0.1 mM, and variable donor concentration from 0 mM to 2 mM.

threshold (see Fig. 5.8).

5.6 Nature of Energy Transfer

Experimental data acquired with bulk liquid and droplets containing R6G and R700 dyes show that energy transfer existed in our experiments. The question is to confirm the non-radiative nature of this energy transfer. Apart from the FRET mechanism, there is also radiative energy transfer mechanism which is the physical phenomenon of energy transfer in the form of electromagnetic radiation [51, 52, 50]. In this mechanism illustrated in Fig. 5.9, photons are emitted by donor molecules and then absorbed by the acceptor molecule. When the pump fluence is increased, more donor photons will be emitted. These photons will be absorbed by the acceptor molecules and this will consequently result in the emission of more acceptor photons. Radiative energy transfer is assisted by the cavity which provides long storage time for the donor photons emitted to the cavity WGMs.

To understand the nature of energy transfer in droplets, we followed control experiments

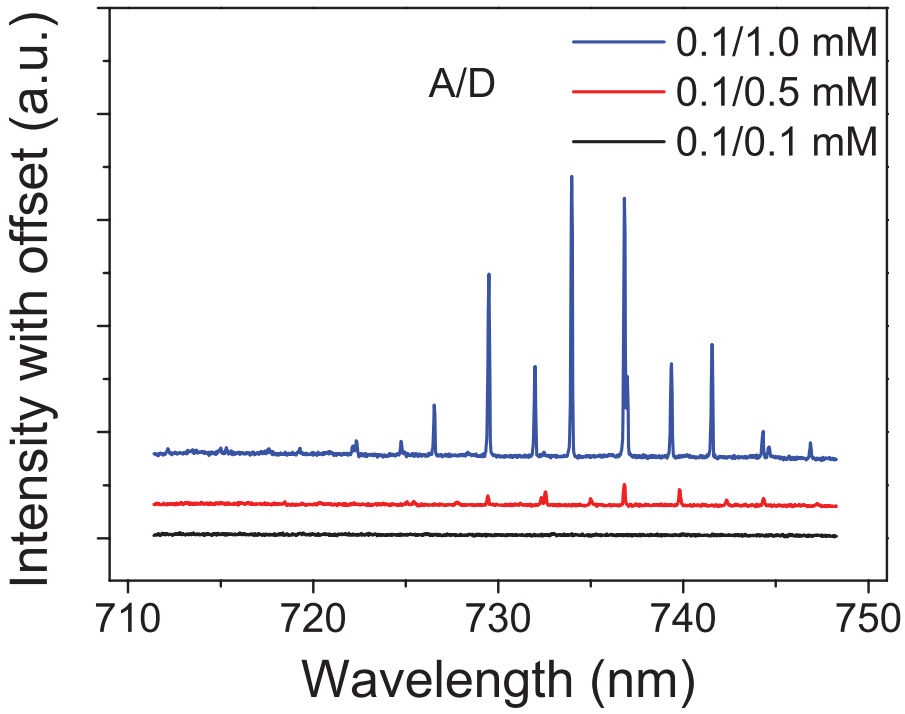

Figure 5.8: Emission spectra in the acceptor lasing region recorded using excitation fluence of 16 mJ/cm^2 for 18 μm diameter droplets doped with 0.1 mM R700 and 0.1 mM, 0.5 mM, and 1.0 mM R6G (bottom to top).

originally reported for Optofluidic Ring Resonator (OFRR) system [6]. First, emission spectra from a single droplet that displayed lasing in both donor and acceptor spectral regions were recorded with different pump fluence. The lasing spectra recorded from a 19 μm diameter microdroplet with 0.1 mM acceptor and 1.0 mM donor concentrations at three different pump fluences are shown in Fig. 5.10. The threshold pump fluence measured for these droplets was 9.3 mJ/cm^2 for acceptor lasing and 132 mJ/cm^2 for donor lasing. When the pump fluence was increased from 75 mJ/cm^2 (below the donor lasing threshold), to 155 mJ/cm^2 (near the donor lasing threshold), and 255 mJ/cm^2 (above the donor lasing threshold), the acceptor lasing peak intensities did not change much while the donor lasing peaks increased as shown in Fig. 5.10.

For the three given pump fluences, effective photon conversion efficiencies, γ, from the donor to the acceptor lasing were calculated by this expression

$$\gamma = (1 + F_{D_{WGM}}/F_{A_{WGM}})^{-1} \tag{5.4}$$

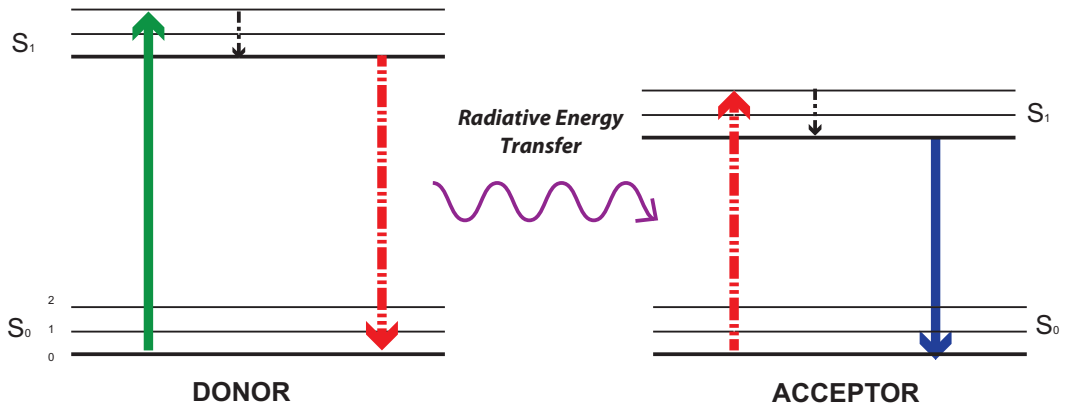

Figure 5.9: Radiative Energy Transfer

where $F_{D_{WGM}}$ and $F_{A_{WGM}}$ are the total intensities above the background level of the lasing WGMs in the donor and acceptor spectral regions, respectively.

Calculations gave effective photon conversion efficiencies ,γ, equal to 100%, 81% and 66% for the shown spectra with the pump fluences that were 43% below, 16% above, and 92% above the donor lasing threshold, respectively. At the lowest excitation fluence, donor lasing is not observed which corresponds to efficient energy transfer to acceptor molecules. As excitation fluence is increased, donor lasing eventually appears with increasing intensity whereas the acceptor lasing intensity remains approximately constant. This behavior is not consistent with pure radiative energy transfer between the donor and acceptor molecules as in such a case, we would expect to see an increase in the acceptor lasing emission triggered by increased density of donor photons in the cavity. Decrease of γ with the increasing pump fluence indicates competition between non-radiative energy transfer from the donor to the acceptor and direct lasing emission from the donor that becomes dominant at high pump fluences.

For the second demonstration, lasing in droplets of similar size ($\sim$19 μm), identical acceptor concentration (0.1 mM), identical pump fluence (480 mJ/cm^2) and different donor concentrations (0.7 mM, 1.0 mM and 1.5 mM) was studied as illustrated in Fig. 5.11. In

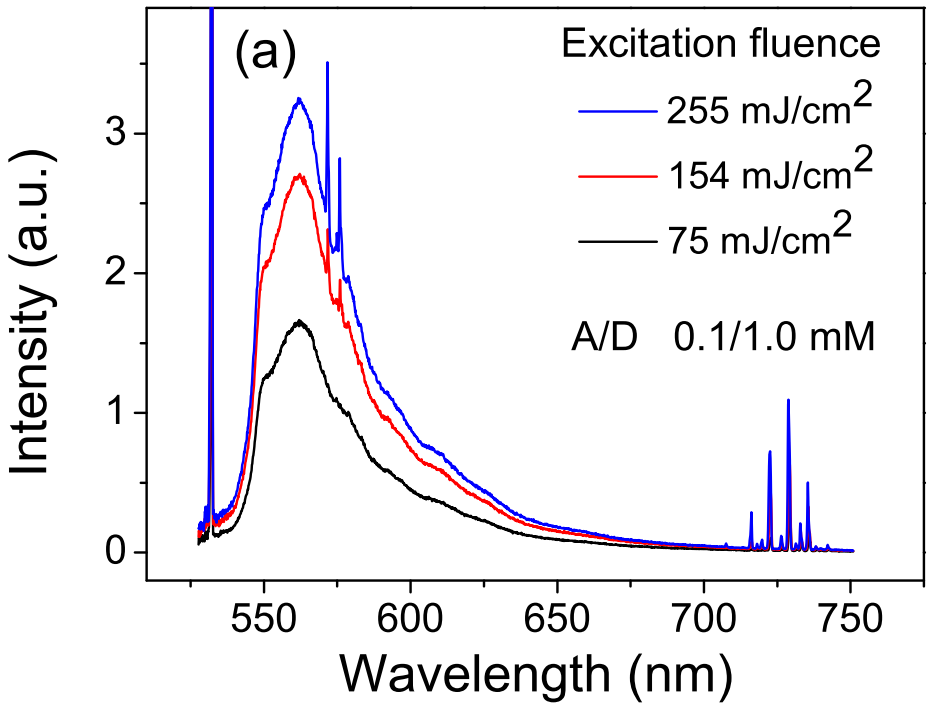

Figure 5.10: Acceptor and donor lasing emission for a 19 μm diameter droplet with 0.1 mM R700 and 1.0 mM R6G excited with 75 mJ/cm^2, 154 mJ/cm^2, and 255 mJ/cm^2 pump fluence. Threshold pump fluence for donor lasing was 132 mJ/cm^2.

these experiments, the donor lasing intensity increased with increasing donor concentration whereas the acceptor lasing intensity did not grow proportionally. Effective photon conversion efficiencies, γ, were calculated as (76%, 68% and 62%) for the donor concentrations 0.7 mM, 1.0 mM and 1.5 mM respectively. Similar to experiments with increasing pump power shown in Fig. 5.10 , this shows the dominance of the non-radiative FRET over the cavity-assisted radiative energy transfer as γ is expected to be independent of the donor concentration for radiative energy transfer [51].

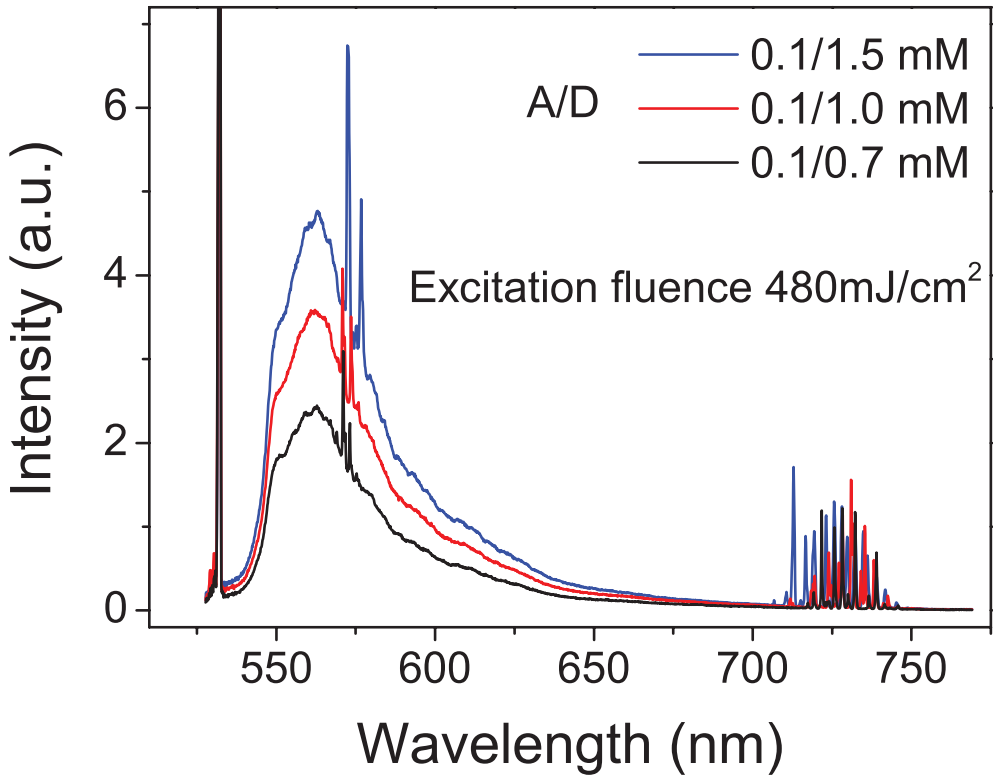

Figure 5.11: Lasing emission spectra for three droplets with similar diameter (19 μm), identical acceptor concentration (0.1 mM) and pump fluence (480 mJ/cm^2), and different donor concentrations (0.7 mM, 1.0 mM and 1.5 mM).

Chapter 6

CONCLUSION

In this thesis, we demonstrated optofluidic microlasers using highly efficient non-radiative Förster resonance energy transfer (FRET) for pumping of the laser gain medium formed by a FRET donor-acceptor pair. In order to provide optical feedback, the gain medium was suspended in liquid microcavities formed by glycerol/water/ethylene glycol microdroplets deposited on a superhydrophobic surface. The lasing is in the emission band of the acceptor as a result of efficient FRET coupling between the acceptor and donor molecules after donor excitation by a pulsed laser was observed and characterized. In addition to experiments, the behavior of lasers based on a mixture of donor and acceptor dyes serving as an active medium was studied theoretically using rate-equation model which provided characteristic features of the output pulses of energy-transfer lasers as a function of donor and acceptor concentration and pump power.

First, basic characteristics of the selected donor-acceptor pair in bulk solution (i.e Förster radius and FRET efficiency) were determined. Afterward, the spectral properties and pump threshold of lasing from microdroplets containing donor and acceptor dyes were studied. The lasing threshold was tuned by changing concentration of both donor and acceptor molecules in the droplet and threshold as low as 6.3 $mJ\ cm^{-2}$ was observed. Finally, the nature of the energy transfer in the lasing microdroplets was verified by changing parameters such as excitation fluence and concentration of donor molecules. These two sets of experiment provided evidence for dominance of non-radiative energy transfer over radiative energy transfer. Demonstration of efficient FRET lasing in droplet-based resonators represents the first step towards applications of the droplet lasers as optical resonant cavities in highly sensitive biological and chemical detection, and the development of photonic devices [53].

APPENDIX A

MATLAB CODE FOR FIGURE 4.1-4.4

```
%Main Code
clc
clear all
close all
global I0 t0 FWHM c N_d N_a tau_d tau_a n np
global omega_d omega_a sigma_pd sigma_pa hp lambda_l lambda_a
global sigma_edl sigma_aal sigma_eal sigma_eaa b L V S kf

hp=6.62606957e-34;     %Planck Constant J.s
c=3e10;                %Speed of light
lambda_l=560e-7;       %Lasing Wavelength
lambda_a=655e-7;       %Lasing Wavelength of acceptor
t0=10e-9;
FWHM=9*10^-9;
%%
N_a=0.3e+18;           %Acceptor Concentration
N_d=1.8e+18;           %Donor Concentration
%%
tau_d=4e-9;            %Donor Lifetime
tau_a=3.3e-9;          %Acceptor Lifetime
n=1.328;               %Refractive index of the solvent
np=1.52;               %Refractive index of the prism
b=0.02;                %Height of the transversely excited region
L=0.9;                 %Length of the transversely excited region
V=0.4;                 %Visibility of the interference pattern
%%
omega_d=1.273e-9;      %Factor determining the fraction of the spon by donor
omega_a=0.255e-6;      %Factor determining the fraction of the spon by donor
%%
sigma_pd=3.4200e-16;  %Absorbtion cross section of donor dye at the
pumping wavelength

sigma_pa=0.0510e-16;  %Absorbtion cross section of acceptpr dye at the
pumping wavelength

sigma_edl=3.7800e-16; %Emission cross section of donor dye molecules at
their lasing wavelength of donor

sigma_aal=0.1558e-16;  %Ground state absorption cross section of acceptor
dye molecules at their lasing wavelength

sigma_eal=0.036e-16;   %Emission cross section of acceptor dye molecules
at their lasing wavelength of donor

sigma_eaa=6.900e-16;   %Emission cross section of acceptor dye molecules at
their lasing wavelength

a=1/(N_d*sigma_pd-N_a*sigma_pa);%Penetration depth
%%
```

```
pp=0;RR=0; Z=7; W=1; Y=0.5;
 for kk=W:Y:Z
     I0 = 1e22*kk;
%options = odeset('RelTol',1e-4,'AbsTol',[1e-4 1e-4 1e-5 1e-5]);
[T,H] = ode15s(@FRET,[0 20e-9],[0 0 0 0]);
%%
pp=pp+1;
Pout_d=(hp*c*L*a*b/lambda_1/2)*(H(:,2)./(max( n * L^3 * (
H(:,1)*(sigma_edl)*V).^2 / (8*c* pi^2)  , n*L/10/c))); % units J/s pr Watt

Pout_a=(hp*c*L*a*b/lambda_a/2)*(H(:,4)./(max( n * L^3 * (
H(:,1)*(sigma_edl)*V).^2 / (8*c* pi^2)  , n*L/10/c))); % units J/s pr Watt

E_d(pp)=sum(diff(T).*(Pout_d(1:end-1,1)+Pout_d(2:end,1))/2);
E_a(pp)=sum(diff(T).*(Pout_a(1:end-1,1)+Pout_a(2:end,1))/2);

%% For Donor
figure(1)
plot(T,Pout_d);
xlabel('Time');
ylabel('Pout_d(t)');
title('Changes in Input Power');
filename= 'Pout_Donor_FRET.gif';
drawnow
frame = getframe(1);
im = frame2im(frame);
[imind,cm] = rgb2ind(im,256);
if kk == 1;
imwrite(imind,cm,filename,'gif', 'Loopcount',inf);
else
imwrite(imind,cm,filename,'gif','WriteMode','append');
end

%% For Acceptor
figure(2)
plot(T,Pout_a);
xlabel('Time');
ylabel('Pout_a-Abs(t)');
title('Changes in Input Power');
filename= 'Pout_Acc_FRET.gif';
drawnow
frame1 = getframe(2);
im1 = frame2im(frame1);
[imind1,cm] = rgb2ind(im1,256);
if kk == 1;
imwrite(imind1,cm,filename,'gif', 'Loopcount',inf);
else
imwrite(imind1,cm,filename,'gif','WriteMode','append');
end
 end
```

```
%Threshold Analysis from Laser Dye
figure(3)
plot(I0*(W:Y:Z),E_d,'*')
xlabel('Excitation Pump');
ylabel('Intensity');
title('Threshold');

%% Threshold Analysis from Saturable Absorber
figure(4)
plot(I0*(W:Y:Z),E_a,'*')
xlabel('Excitation Pump');
ylabel('Intensity');
title('Threshold');

%%Supplementary Function "Coupled Rate Equations"
function dH=FRET(t,h)
dH=zeros(4,1);
global I0 t0 FWHM c N_d N_a tau_d tau_a n np
global omega_d omega_a sigma_pd sigma_pa hp lambda_l lambda_a
global sigma_edl sigma_aal sigma_eal sigma_eaa b L V S kf
%%
Ip= I0 * exp(2.3548^2*(-(t-t0).^2)/FWHM^2 /2); %Spatially average pumped
power
kf=1.56e-10;
tau_c= max(n* L^3 * (h(1)*(sigma_edl)*V)^2 / (8*c* pi^2) , n*L/10/c);

%% The rate of change of donor dye molecules;
dH(1)=Ip*sigma_pd*(N_d-h(1))-((sigma_edl*c*h(1)*h(2))/n)-h(1)/tau_d-kf;

%% The rate of change of donor photon density
t1=((sigma_edl*c*h(1)*h(2))/n);
t2=h(2)/tau_c;
t3=omega_d*h(1)/tau_d;
t4=sigma_aal*c*(N_a-h(3))*h(2)/n;
t5=((sigma_eal*c*h(3)*h(2))/n);
dH(2)=t1-t2+t3-t4+t5; % - or (+) t5

%% The rate of change of acceptor dye molecules
t6=Ip*sigma_pa*(N_a-h(3));
t7=((sigma_eaa*c*h(3)*h(4))/n);
t8=(h(3)/tau_a);
t9=(sigma_aal*c*(N_a-h(3))*h(2)/n);
t10=((sigma_eal*c*h(3)*h(2))/n);
dH(3)=t6-t7-t8+t9-t10+kf; % (-) or + t10

%% The rate of change of acceptor photon density
dH(4)=((sigma_eaa*c*h(3)*h(4))/n)-h(4)/tau_c+omega_a*h(3)/tau_a;
```

BIBLIOGRAPHY

[1] D. Psaltis, S. R. Quake, and C. Yang, "Developing optofluidic technology through the fusion of microfluidics and optics," Nature **442**, 381–386 (2006).

[2] M. Li and C. K. Ober, "Block copolymer patterns and templates," Materials Today **9**, 30–39 (2006).

[3] Y. Sun, S. I. Shopova, C.-S. Wu, S. Arnold, and X. Fan, "Bioinspired optofluidic fret lasers via dna scaffolds," National Academy of Sciences **107**, 16039–16042 (2010).

[4] J. Schfer, J. P. Mondia, R. Sharma, Z. H. Lu, A. S. Susha, A. L. Rogach, and L. J. Wang, "Quantum dot microdrop laser," Nano **8**, 1709–1712 (2008).

[5] M. C. Gather and S. H. Yun, "Single-cell biological lasers," Nat Photon **5**, 406–410 (2011).

[6] S. I. Shopova, J. M. Cupps, P. Zhang, E. P. Henderson, S. Lacey, and X. Fan, "Optofluidic ring resonator lasers based on highly efficient resonant energy transfer," Optics Express **15**, 12735–12742 (2007).

[7] M. C. Gather and S. H. Yun, "Lasing from escherichia coli bacteria genetically programmed to express green fluorescent protein," Opt. Lett. **36**, 3299–3301 (2011).

[8] X. Fan and S. H. Yun, "The potential of optofluidic biolasers," Nat Meth **11**, 141–147 (2014).

[9] Y. Sun and X. Fan, "Distinguishing dna by analog-to-digital-like conversion by using optofluidic lasers," Angewandte Chemie International Edition **51**, 1236–1239 (2012).

[10] S.-X. Qian, J. B. Snow, H. M. Tzeng, and R. K. Chang, "Lasing droplets: Highlighting the liquid-air interface by laser emission," Science **231**, 486 (1986).

[11] V. V. Datsyuk, "Optics of microdroplets," J. Mol. Liq. **84**, 1308–1316 (2001).

[12] A. Kiraz, A. Kurt, M. A. Dündar, and A. L. Demirel, "Simple largely tunable optical microcavity," Appl. Phys. Lett. **89**, 081118 (2006).

[13] A. Sennaroglu, A. Kiraz, M. A. Dündar, A. Kurt, and A. L. Demirel, "Raman lasing near 630 nm from stationary glycerol-water microdroplets on a superhydrophobic surface," Opt. Lett. **32**, 2197–2199 (2007).

[14] A. Kiraz, A. Sennaroglu, S. Doganay, M. A. Dundar, A. Kurt, H. Kalaycoglu, and A. L. Demirel, "Lasing from single, stationary, dye-doped glycerol/water microdroplets located on a superhydrophobic surface," Opt. Commun. **276**, 145–148 (2007).

[15] F. Vollmer, D. Braun, A. Libchaber, M. Khoshsima, I. Teraoka, and S. Arnold, "Protein detection by optical shift of a resonant microcavity," Applied Physics Letters **80**, 4057–4059 (2002).

[16] F. Vollmer and L. Yang, "Label-free detection with high-q microcavities: a review of biosensing mechanisms for integrated devices," Nanophotonics **1**, 267–291 (2012).

[17] S. Arnold, M. Neuman, and A. B. Pluchino, "Molecular spectroscopy of a single aerosol particle," Opt. Lett. **9**, 4–6 (1984).

[18] A. Ashkin and J. M. Dziedzic, "Optical levitation of liquid drops by radiation pressure," Science **187**, 1073 (1975).

[19] T. Förster, "Transfer mechanisms of electronic excitation," Discuss. Faraday Soc. **27**, 7–17 (1959).

[20] A. Clebsch, Journal fr Mathematik **Band 61, Heft 3** (1862).

[21] L. Lorenz, "Det kongelige danske videnskabernes selskabs skrifter," **6. Raekke, 6. Bind 1, 1** (1890).

[22] P. Debye, Annalen der Physik **Band 30. No. 1, 57** (1909).

[23] B. Rayleigh, John William Strutt, *Scientific papers* (Cambridge : University Press, 1920).

[24] G. Grehan, B. Maheu, and G. Gouesbet, "Scattering of laser beams by mie scatter centers: numerical results using a localized approximation," Appl. Opt. **25**, 3539–3548 (1986).

[25] G. Mie, "Beitrage zer optik truber meiden speziell kolloidaler metallosungen," Ann. Phys. (Leipzig) **25**, 377–445 (1908).

[26] A. Jonas, "Use of standing electromagnetic wave for manipulation of micron and submicron-sized objects," Ph.D. thesis, BRNO UNIVERSITY OF TECHNOLOGY (2001).

[27] J. P. Barton, D. R. Alexander, and S. A. Schaub, "Internal fields of a spherical particle illuminated by a tightly focused laser beam: Focal point positioning effects at resonance," J. Appl. Phys. **65**, 2900–2906 (1989).

[28] J. P. Barton, D. R. Alexander, and S. A. Schaub, "Internal and near-surface electromagnetic fields for a spherical particle irradiated by a focused laser beam," J. Appl. Phys. **64**, 1632–1639 (1988).

[29] G. C. Righini, Y. Dumeige, P. Feron, M. Ferrari, G. N. Conti, D. Ristic, and S. Soria, "Whispering gallery mode microresonators: Fundamentals and applications," Rivista Del Nuovo Cimento **34**, 435–488 (2011).

[30] Y. Karadag, "Ultrahigh resolution optical spectroscopy of liquid microdroplets using tapered optical fiber waveguides," Ph.D. thesis, Koc University (2013).

[31] M. H. Fields, J. Popp, and R. K. Chang, "Nonlinear optics in microspheres," in "Progress in Optics," , vol. 41, E. Wolf, ed. (Elsevier, 2000), pp. 1–95.

[32] N. J. Emptage, "Fluorescent imaging in living systems," Current Opinion in Pharmacology **1**, 521 – 525 (2001).

[33] B. Valeur, *Molecular Fluorescence Principles and Applications* (Wiley-VCH, 2002).

[34] J. R. Lakowicz, *Principles of Fluorescence Spectroscopy* (Springer, 2006).

[35] L. Stryer and R. P. Haugland, "Energy transfer: A spectroscopic ruler," National Academy of Sciences **68** (1967).

[36] L. R. Joseph, *Principles of Fluorescence Spectroscopy* (Plenum Press Newyork and London, 1986).

[37] R. T. Williams and J. W. Bridges, "Fluorescence of solutions: A review," Journal of Clinical Pat **17(4)**, 371394 (1964).

[38] G. Stokes, "On the change of refrangibility of light," Phil Trans R Soc (London) **142**, 463–562 (1852).

[39] L. Stryer, "Fluorescence energy-transfer as a spectroscopic ruler," Ann. Review of Biochemistry **47**, 819–846 (1978).

[40] R. Clegg, "Fluorescence resonance energy transfer. fluorescence imaging spectroscopy and microscopy," John Wiley & Sons Inc **137**, 179251 (1996).

[41] B.-K. Fung and Lubert, "Surface density determination in membranes by fluorescence energy transfer," Biochemisty **17(24)**, 5241–5248 (1978).

[42] H. Kogelnik and C. V. Shank, "Stimulated emission in a periodic structure," Applied Physics Letters **18**, 152–154 (1971).

[43] J. Hebling, "20 ps pulse generation by an excimer laser pumped double self-q-switched distributed feedback dye laser," Appl. Phys. B **47**, 267 (1988).

[44] J. Hebling, J. Seres, Z. Bor, and B. Racz, "Dye laser pulse shortening and stabilization by q-switching," Optical and Quantum Electronics **22**, 375–384 (1990).

[45] G. Peterson and B. Snavely, Bull. Am. Phys. Soc **13**, 397 (1968).

[46] A. Dienes and M. Madden, J. App **44** (1973).

[47] M. B. Ahamed and P. Palanisamy, "Nd:yag laser pumped energy transfer distributed feedback dye laser in rhodamine 6g and acid blue 7 dye mixture," Optics Communications **213**, 67 – 80 (2002).

[48] M. Y. Yüce, A. L. Demirel, and F. Menzel, "Tuning the surface hydrophobicity of polymer/nanoparticle composite films in the wenzel regime by composition," Langmuir **21**, 5073 (2005).

[49] A. Checco, P. Guenoun, and J. Daillant, "Nonlinear dependence of the contact angle of nanodroplets on contact line curvature," Phys. Rev. Lett. **91**, 186101 (2003).

[50] E. Özelci, M. Aas, A. Jonás, and A. Kiraz, "Optofluidic fret microlasers based on surface-supported liquid microdroplets," Laser Physics Letters **11**, 045802 (2014).

[51] S. Arnold and L. M. Folan, "Energy transfer and the photon lifetime within an aerosol particle," Opt. Lett. **14**, 387–389 (1989).

[52] A. Kiraz, S. Doanay, A. Kurt, and A. L. Demirel, "Enhanced energy transfer in single glycerol/water microdroplets standing on a superhydrophobic surface," Chem. Phys. L **444**, 181–185 (2007).

[53] I. M. White, H. Oveys, and X. Fan, "Liquid-core optical ring-resonator sensors," Opt. Lett. **31**, 1319–1321 (2006).

VITA

Ersan Özelci was born in Kastamonu, Turkey on June 15, 1990. He received his B.Sc. degree in Physics Engineering from Istanbul Technical University, Istanbul, Turkey, in 2012. His bachelor thesis work was titled as *Determination of the Grain Size Distribution Using MATLAB Programming*. He later joined the M.Sc. program in Optoelectronics and Photonics Engineering at Koç University, Istanbul, Turkey in 2012. His M. Sc. degree thesis is *Optofluidic Microlasers Based on Non-Radiative Energy Transfer in Surface-supported Liquid Microdroplets*. He orally presented this work in international conference, Conference on Lasers and Electro-Optics (CLEO) 2014. He is a student member of International Society for Optical Engineering (SPIE) and Optical Society of America(OSA).

List of Publications

1. **E. Özelci**, M. Aas, A. Jonás, and A. Kiraz "Optofluidic FRET microlasers based on surface supported liquid microdroplets" Laser Physics Letters, 11(4):045802, 2014.

2. M. Aas, **E. Özelci**, A. Jonás, A. Kiraz, H. Liu, C. Fan, Q. Chen, and X. Fan "FRET lasing from self-assembled DNA tetrahedral nanostructures suspended in optouidic droplet resonators" Eur. Phys. J. Special Topics, 2014.

3. **E. Özelci**, M. Aas, Jonás, and A. Kiraz, Miniature droplet-based fret lasers stabilized by superhydrophobic surfaces, in CLEO: 2014, (Optical Society of America, 2014), p. STh3H.4.